EUROPEAN ORGANIZATION FOR NUCLEAR RESEARCH (CERN)

CERN-EP-2022-113
2022/06/21

CMS-HIG-21-002

Search for Higgs boson pairs decaying to WWWW, WW$\tau\tau$, and $\tau\tau\tau\tau$ in proton-proton collisions at $\sqrt{s} = 13$ TeV

The CMS Collaboration

Abstract

The results of a search for Higgs boson pair (HH) production in the WWWW, WW$\tau\tau$, and $\tau\tau\tau\tau$ decay modes are presented. The search uses 138 fb^{-1} of proton-proton collision data recorded by the CMS experiment at the LHC at a center-of-mass energy of 13 TeV from 2016 to 2018. Analyzed events contain two, three, or four reconstructed leptons, including electrons, muons, and hadronically decaying tau leptons. No evidence for a signal is found in the data. Upper limits are set on the cross section for nonresonant HH production, as well as resonant production in which a new heavy particle decays to a pair of Higgs bosons. For nonresonant production, the observed (expected) upper limit on the cross section at 95% confidence level (CL) is 21.3 (19.4) times the standard model (SM) prediction. The observed (expected) ratio of the trilinear Higgs boson self-coupling to its value in the SM is constrained to be within the interval -6.9 to 11.1 (-6.9 to 11.7) at 95% CL, and limits are set on a variety of new-physics models using an effective field theory approach. The observed (expected) limits on the cross section for resonant HH production amount to 0.18–0.90 (0.08–1.06) pb at 95% CL for new heavy-particle masses in the range 250–1000 GeV.

Submitted to the Journal of High Energy Physics

1 Introduction

Since the discovery of the Higgs (H) boson [1–3], many of its properties have already been measured with high precision [4–6]. One important property that remains largely unknown is the H boson self-coupling. A precise measurement of this coupling is necessary to determine the shape of the Higgs potential, and thus verify that the mechanism breaking the electroweak gauge symmetry is indeed the Higgs mechanism [7–12] of the standard model (SM) [13–15]. The SM predicts the existence of trilinear as well as quartic H boson self-couplings. Due to the very low cross section for triple H boson production, the quartic self-coupling will not be experimentally accessible at the CERN LHC, even with the full integrated luminosity of 3000 fb^{-1} scheduled to be delivered after the high-luminosity LHC upgrade [16, 17]. The strength of the trilinear self-coupling, however, can be determined using measurements of H boson pair (HH) production.

In the SM, most HH pairs are produced in two types of processes. The Feynman diagrams for the dominant "gluon fusion" (ggHH) process at leading order (LO) in perturbative quantum chromodynamics (QCD) are shown in Fig. 1. The left "triangle" diagram amplitude varies proportionally to the H boson self-coupling (λ) and the Yukawa coupling of the top quark (y_t), while the right "box" diagram amplitude is insensitive to λ and varies as y_t^2. The triangle and box diagrams interfere destructively, so the ggHH cross section exhibits a strong dependence on λ and y_t. The ratios of λ and y_t to their SM expectations are denoted as κ_λ and κ_t, respectively. By definition, these "coupling strength modifiers" have values $\kappa_\lambda = 1$ and $\kappa_t = 1$ in the SM. The ggHH cross section in the SM has been computed to be $31.1^{+2.1}_{-7.2}$ fb at next-to-next-to-LO (NNLO) accuracy in QCD using the $\text{FT}_{\text{approx}}$ scheme, in which the true top quark mass is used for the real radiation matrix elements, while the virtual part is computed using an infinite top quark mass [18]. The SM cross section for the subdominant "vector boson fusion" (qqHH) process has been computed at next-to-NNLO accuracy in QCD and amounts to 1.73 ± 0.04 fb [19].

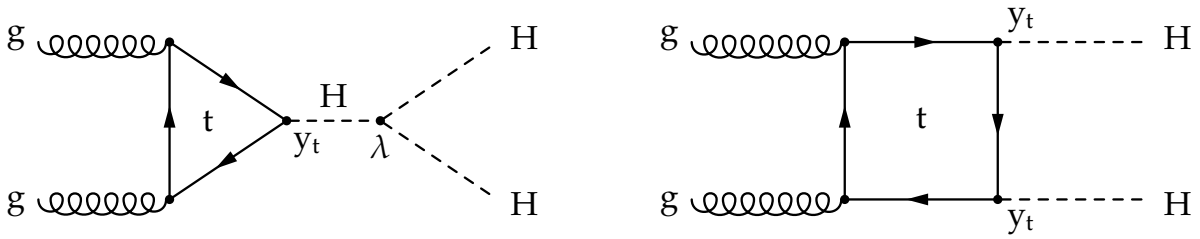

Figure 1: Leading order Feynman diagrams for SM nonresonant HH production via gluon fusion, including the "triangle" diagram (left) and the "box" diagram (right).

Deviations of these coupling strength modifiers from unity not only affect the rate of HH production, but also the kinematic distributions of the HH signal. The HH invariant mass (m_{HH}) is particularly sensitive to changes in κ_λ and κ_t, as these couplings affect the triangle and box diagram amplitudes differently. Because SM ggHH and qqHH production do not include a heavy resonant particle, and typically result in a broad m_{HH} distribution, they are referred to as "nonresonant". Changes in κ_λ and κ_t also influence the rate of single Higgs boson production as well as the Higgs boson decay branching fractions [20, 21].

The presence of undiscovered particles or interactions, predicted by a variety of theoretical models beyond the SM, may alter the HH production rate as well as observable kinematic distributions. Such particles could give rise to loop diagrams similar to those shown in the upper row of Fig. 1. These diagrams may significantly enhance the HH production rate, as they occur

at the same loop level as HH production in the SM. Since no particles beyond those predicted by the SM have been observed so far, their mass may be at the TeV scale or higher, well above the scale of electroweak symmetry breaking. Loop contributions of such heavy particles can be approximated as contact interactions with the H boson using an effective field theory (EFT) approach [22, 23]. Following Ref. [24], the contact interactions relevant for HH production are parametrized by the couplings c_g, c_{2g}, and c_2, referring to the interactions between two gluons and one H boson, two gluons and two H bosons, and two top quarks and two H bosons, respectively. The corresponding Feynman diagrams for ggHH production are shown in Fig. 2. The LO diagrams for qqHH production contain no gluons or top quarks, so the impacts of c_g, c_{2g}, and c_2 are only considered in the ggHH signal in this publication.

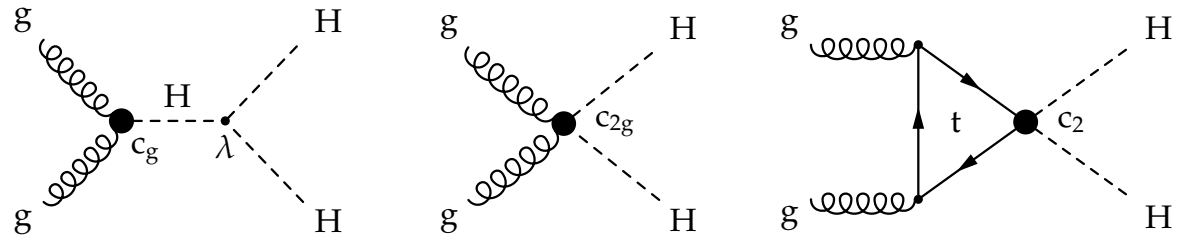

Figure 2: Leading order Feynman diagrams for nonresonant HH production via gluon fusion in an EFT approach, where loop-mediated contact interactions between (left) two gluons and one H boson, (middle) two gluons and two H bosons, and (right) two top quarks and two H bosons are parametrized by three effective couplings: c_g, c_{2g}, and c_2.

An excess of HH signal events may also result from decays of new heavy particles, denoted as X, into pairs of H bosons. Various theoretical models of new physics postulate such decays, in particular two-Higgs-doublet models [25, 26], composite-Higgs models [27, 28], Higgs portal models [29, 30], and models inspired by warped extra dimensions [31]. In the last class of models, the new heavy particles may have spin 0 ("radions") or spin 2 ("gravitons") [32]. In this paper, the resulting "resonant" HH production is sought for mass values of X from 250 to 1000 GeV, and the width of X is assumed to be negligible compared to the experimental resolution in m_{HH}. This creates a peak in the reconstructed m_{HH} distribution around the mass m_{X} of the resonance. The Feynman diagram for this process is shown in Fig. 3. Resonance masses above 1 TeV are strongly constrained by searches targeting H boson decays to bottom quarks [33, 34], as the selection and reconstruction efficiency, in particular of the trigger, for hadronic decays increases and relevant backgrounds decrease with energy.

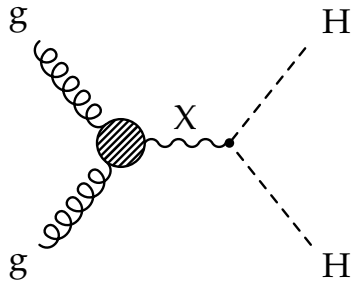

Figure 3: Leading order Feynman diagram for resonant HH production.

In this paper, we present a search for nonresonant as well as resonant HH production in final states with multiple reconstructed leptons, i.e., electrons (e), muons (μ), or hadronically decaying tau leptons (τ_{h}). The search is based on LHC proton-proton (pp) collision data recorded by the CMS experiment at a center-of-mass energy of 13 TeV, corresponding to an integrated

luminosity of 138 fb^{-1}. Signal candidate events are subdivided into seven mutually exclusive "search categories" based on ℓ (e, μ) and τ_h multiplicity: two same-sign ℓ with less than two τ_h (2ℓss), three ℓ with no τ_h (3ℓ), four ℓ (4ℓ), three ℓ with one additional τ_h ($3\ell + 1\tau_\text{h}$), two ℓ with two τ_h ($2\ell + 2\tau_\text{h}$), one ℓ with three τ_h ($1\ell + 3\tau_\text{h}$), or four τ_h with no ℓ ($4\tau_\text{h}$). In final states with a total of four ℓ and τ_h, the charge sum of all ℓ and τ_h candidates is required to be zero. The seven search categories target HH signal events in which the H boson pair decays into WWWW, WW$\tau\tau$, or $\tau\tau\tau\tau$. Multivariate analysis (MVA) methods are used to distinguish the HH signal from backgrounds.

Phenomenological studies of the prospects for discovering HH signal in the WWWW decay mode are documented in Refs. [35–39]. The ATLAS Collaboration published the results of a search for nonresonant as well as resonant HH production in this decay mode based on 36 fb^{-1} of pp collision data recorded at $\sqrt{s} = 13$ TeV [40], placing an upper limit of 160 times the SM predicted cross section for nonresonant HH production at 95% confidence level (CL). This paper presents the first search for H boson pairs decaying to WW$\tau\tau$ and $\tau\tau\tau\tau$. Searches for HH production in pp collisions at $\sqrt{s} = 7, 8$, and 13 TeV have previously been performed by the CMS and ATLAS Collaborations in the decay modes bb$\gamma\gamma$ [41, 42], bbbb [34, 43, 44], bb$\tau\tau$ [45, 46], bbWW [47, 48], and WW$\gamma\gamma$ [49]. Limits on HH production obtained from a combination of some of these analyses have been published by the CMS and ATLAS Collaborations [50, 51].

Searches targeting the bb$\gamma\gamma$ [41] and bbbb [43] final states in CMS, and bb$\gamma\gamma$ [42] in ATLAS, provide the strongest constraints on nonresonant HH production to date, with 95% CL upper limits ranging from 3.9 to 7.7 times the SM predicted cross section. The corresponding lower bounds on κ_λ vary from -3.3 to -1.5, with upper bounds between 6.7 and 9.4. The ATLAS bb$\gamma\gamma$ analysis places a 95% CL upper limit of 0.64 pb on resonant HH production with a mass around 250 GeV, and lower limits for higher masses, down to 0.05 pb at 1 TeV. The only published HH search using an EFT approach comes from CMS in the bb$\gamma\gamma$ final state, with 95% CL upper limits on the HH production cross section ranging from 0.1 to 0.6 pb, depending on the EFT scenario [41].

The paper is structured as follows. A brief overview of the CMS detector is given in Section 2. In Section 3, we list the data sets and simulation samples used. The reconstruction of e, μ, τ_h, and jets, along with various kinematic observables, is detailed in Section 4. This is followed by a description, in Section 5, of the event selection criteria defining the seven search categories. The multivariate methods used to distinguish the HH signal from backgrounds are detailed in Section 6. The estimation of these backgrounds is described in Section 7, followed by an outline of the relevant systematic uncertainties in Section 8. The statistical procedure used to extract limits on the HH production rate in the SM, as well as constraints on SM coupling strengths, EFT benchmark scenarios, and resonant HH production rates are presented in Section 9. The paper concludes with a summary in Section 10.

2 The CMS detector

The central feature of the CMS apparatus is a superconducting solenoid of 6 m internal diameter, providing a magnetic field of 3.8 T. Within the solenoid volume are a silicon pixel and strip tracker, a lead tungstate crystal electromagnetic calorimeter (ECAL), and a brass and scintillator hadron calorimeter (HCAL), each composed of one barrel and two endcap sections. The silicon tracker measures charged particles within the pseudorapidity range $|\eta| < 2.5$ for data recorded in 2016, and within the range $|\eta| < 3.0$ for data recorded in 2017 and 2018. The ECAL is a fine-grained hermetic calorimeter with quasi-projective geometry, and is divided into a

barrel region covering $|\eta| < 1.5$, and two endcaps that extend to $|\eta| = 3.0$. The HCAL barrel and endcaps similarly cover the region $|\eta| < 3.0$. Forward calorimeters extend beyond these endcaps to $|\eta| = 5.0$. Muons are detected within the range $|\eta| < 2.4$ by gas-ionization detectors embedded in the steel flux-return yoke outside the solenoid. Collision events of interest are selected using a two-tiered trigger system. The level-1 trigger, composed of custom hardware processors, uses information from the calorimeters and muon detectors to select less than 100 kHz of events from a 40 MHz base event rate, within a fixed latency of 4 μs [52]. The second tier, known as the high-level trigger, is a processor farm which runs a version of the full event reconstruction software optimized for fast processing, and reduces the event rate to around 1 kHz before data storage [53]. A more detailed description of the CMS detector, together with a definition of the coordinate system used and the most relevant kinematic variables, can be found in Ref. [54].

3 Data samples and Monte Carlo simulation

The analyzed pp collision data correspond to an integrated luminosity of 138 fb^{-1}, collected by the CMS detector over three years: 36 fb^{-1} in 2016, 42 fb^{-1} in 2017, and 60 fb^{-1} in 2018 [55–57]. Only the data-taking periods during which all detector components were fully operational are included in the analysis. This analysis uses triggers requiring one or more reconstructed e, μ, or τ_h candidates to be associated with the same collision vertex. The exact triggers and their thresholds varied slightly from year to year because of changes in luminosity and detector conditions, as well as improvements to the trigger algorithms. The transverse momentum (p_T) thresholds imposed by the trigger on the "leading" (highest p_T), "subleading" (second-highest p_T), and third e, μ, or τ_h, and the corresponding η requirements for each year are shown in Table 1. All triggers include identification and isolation requirements on the e, μ, and τ_h candidates [53]. When combined, the triggers achieve an efficiency of 95–100% for simulated SM HH signal events in each of the seven search categories.

Table 1: Selection requirements on p_T and η of reconstructed electrons (e), muons (μ), and hadronically decaying tau leptons (τ_h) applied by the triggers used in this analysis. The trigger p_T thresholds for leading, subleading, and third e, μ, or τ_h are separated by commas. For trigger thresholds that varied over time, the range of variation is indicated.

Trigger	Selection requirements for reconstructed e, μ, and τ_h objects
Single e	$p_\text{T}(\text{e}) > 27$–$35\,\text{GeV}$
Single μ	$p_\text{T}(\mu) > 22$–$27\,\text{GeV}$
Double e	$p_\text{T}(\text{e}) > 23, 12\,\text{GeV}$
e + μ	$p_\text{T}(\text{e}) > 23\,\text{GeV}$, $p_\text{T}(\mu) > 8\,\text{GeV}$
μ + e	$p_\text{T}(\mu) > 23\,\text{GeV}$, $p_\text{T}(\text{e}) > 8$–$12\,\text{GeV}$
Double μ	$p_\text{T}(\mu) > 17, 8\,\text{GeV}$
e + τ_h	$p_\text{T}(\text{e}) > 24\,\text{GeV}$, $p_\text{T}(\tau_\text{h}) > 20$–$30\,\text{GeV}$, $\lvert\eta(\text{e}, \tau_\text{h})\rvert < 2.1$
μ + τ_h	$p_\text{T}(\mu) > 19$–$20\,\text{GeV}$, $p_\text{T}(\tau_\text{h}) > 20$–$27\,\text{GeV}$, $\lvert\eta(\mu, \tau_\text{h})\rvert < 2.1$
Double τ_h	$p_\text{T}(\tau_\text{h}) > 35$–$40\,\text{GeV}$, $\lvert\eta(\tau_\text{h})\rvert < 2.1$
Triple e	$p_\text{T}(\text{e}) > 16, 12, 8\,\text{GeV}$
Two e + μ	$p_\text{T}(\text{e}) > 12, 12\,\text{GeV}$, $p_\text{T}(\mu) > 8\,\text{GeV}$
Two μ + e	$p_\text{T}(\mu) > 9, 9\,\text{GeV}$, $p_\text{T}(\text{e}) > 9\,\text{GeV}$
Triple μ	$p_\text{T}(\mu) > 12, 10, 5\,\text{GeV}$

Monte Carlo (MC) simulated samples are used to model HH signal events and a wide range of SM background processes that produce final states with e, μ, or τ_h. Background MC samples

include processes producing a single W or Z boson, two bosons (WW, WZ, ZZ, Wγ, and Zγ), three bosons (WWW, WWZ, WZZ, ZZZ, and WZγ), a single H boson (via gluon fusion, vector boson fusion, or associated production with a W or Z boson), a single top quark, a top quark-antiquark pair ($\mathrm{t\bar{t}}$), and top quarks associated with one or more bosons ($\mathrm{t\bar{t}W}$, $\mathrm{t\bar{t}Z}$, $\mathrm{t\bar{t}H}$, tHq, and tHW). The WW samples comprise same-sign and opposite-sign WW pairs, including same-sign WW pairs produced by double-parton interactions. All samples that include a H boson were produced for a H boson mass of 125 GeV. Most samples, including the dominant WZ and ZZ backgrounds, were generated at next-to-LO (NLO) and scaled to cross sections computed at NNLO in QCD.

A variety of HH signal samples were generated at LO and at NLO accuracy in QCD to simulate nonresonant HH production, covering the ggHH and qqHH production processes. Each of the H bosons was forced to decay to either WW, ZZ, or $\tau\tau$ in these samples. The LO samples are used for the training of machine learning algorithms, while the NLO samples are used to extract the rate of the HH signal from the data. Separate ggHH samples are produced for SM HH production and for a total of twelve benchmark (BM) scenarios in the EFT approach [24]. These benchmarks, as well as the seven benchmarks from Ref. [58], represent different combinations of κ_λ, κ_t, $\mathrm{c_g}$, $\mathrm{c_{2g}}$, and $\mathrm{c_2}$ values, and are chosen to probe distinct classes of HH kinematic configurations. We will refer to these benchmarks as JHEP04 BM1-12, and JHEP03 BM1-7, respectively. The benchmark JHEP04 BM8 is complemented by a modified version of this benchmark, published in Ref. [59], denoted as JHEP04 BM8a. The parameter values of these twenty BM scenarios are shown in Table 2. The values of the $\mathrm{c_g}$ and $\mathrm{c_{2g}}$ couplings published in Ref. [58] have been scaled by factors of 1.5 and -3, respectively, to convert them to the convention introduced for these couplings in Ref. [24]. In order to increase the number of simulated events and to model kinematic configurations not explicitly generated, such as JHEP03 BM1-7, the ggHH samples are merged and the events in the merged samples are reweighted, using the procedure documented in Ref. [60], to match the distributions in m_HH and $|\cos\theta^*|$ computed at NLO accuracy and published in Ref. [59]. This procedure is applied to the LO and NLO ggHH samples separately. The symbol $\cos\theta^*$ denotes the cosine of the polar angle of one H with respect to the beam axis in the HH rest frame. The qqHH samples are produced only for SM HH production.

Resonant HH production was simulated at LO for both spin-0 (radion) and spin-2 (graviton) scenarios with m_X values of 250, 260, 270, 280, 300, 320, 350, 400, 450, 500, 550, 600, 650, 700, 750, 800, 850, 900, and 1000 GeV.

All MC samples were generated using either MADGRAPH5_aMC@NLO v2.2.2 or v2.3.3 [61, 62], POWHEG v2 [63–79], or PYTHIA v8.2 [80]. The production of HH signal samples with MADGRAPH5_aMC@NLO is based on the work published in Refs. [81, 82]. The parton distribution functions (PDFs) of the proton are modeled using the NNPDF3.0 and NNPDF3.1 PDF sets [83–87]. Parton shower, hadronization processes, and τ decays are modeled by PYTHIA, using the tunes CP5, CUETP8M1, CUETP8M2, or CUETP8M2T4 [88–90], depending on the process and the data-taking period that is being modeled. The matching of matrix elements to parton showers is performed using the MLM scheme [91] for the LO samples and the FxFx scheme [92] for the NLO samples. The interactions of particles with the CMS detector material was simulated in detail using GEANT4 [93]. Simulated events were reconstructed using the same procedure as in data. The response of the trigger is included in the simulation. Additional pp interactions (pileup) were generated with PYTHIA and overlaid on all MC events, with event weights used to match the collision multiplicity to the distribution inferred from data. Residual differences between data and simulation are rectified by applying corrections to simulated events.

Table 2: Parameter values for κ_λ, κ_t, c_2, c_g, and c_{2g} in MC samples modeling twenty benchmark scenarios in the EFT approach, plus SM HH production.

Benchmark	κ_λ	κ_t	c_2	c_g	c_{2g}
JHEP04 BM1	7.5	1.0	-1.0	0.0	0.0
JHEP04 BM2	1.0	1.0	0.5	-0.8	0.6
JHEP04 BM3	1.0	1.0	-1.5	0.0	-0.8
JHEP04 BM4	-3.5	1.5	-3.0	0.0	0.0
JHEP04 BM5	1.0	1.0	0.0	0.8	-1.0
JHEP04 BM6	2.4	1.0	0.0	0.2	-0.2
JHEP04 BM7	5.0	1.0	0.0	0.2	-0.2
JHEP04 BM8	15.0	1.0	0.0	-1.0	1.0
JHEP04 BM8a	1.0	1.0	0.5	4/15	0.0
JHEP04 BM9	1.0	1.0	1.0	-0.6	0.6
JHEP04 BM10	10.0	1.5	-1.0	0.0	0.0
JHEP04 BM11	2.4	1.0	0.0	1.0	-1.0
JHEP04 BM12	15.0	1.0	1.0	0.0	0.0
JHEP03 BM1	3.94	0.94	$-1/3$	0.75	-1
JHEP03 BM2	6.84	0.61	1/3	0	1
JHEP03 BM3	2.21	1.05	$-1/3$	0.75	-1.5
JHEP03 BM4	2.79	0.61	1/3	-0.75	-0.5
JHEP03 BM5	3.95	1.17	$-1/3$	0.25	1.5
JHEP03 BM6	5.68	0.83	1/3	-0.75	-1
JHEP03 BM7	-0.10	0.94	1	0.25	0.5
SM	1.0	1.0	0.0	0.0	0.0

4 Event reconstruction

The CMS particle-flow (PF) algorithm [94] aims to reconstruct and identify each individual particle in an event, using an optimized combination of information from the various elements of the CMS detector. The particles are subsequently classified into five mutually exclusive types: electrons, muons, photons, and charged and neutral hadrons. These particles are then combined to reconstruct hadronic τ decays, jets, and the missing transverse momentum in the event.

The candidate vertex with the largest value of summed physics-object p_T^2 is taken to be the primary pp interaction vertex. The physics objects used for this determination are the jets, clustered using the infrared and collinear safe anti-k_T algorithm [95, 96], with the tracks assigned to candidate vertices as inputs, and the associated missing transverse momentum, taken as the negative vector sum of the p_T of those jets.

Electrons are reconstructed within the geometric acceptance of the tracking detectors ($|\eta| < 2.5$) by combining information from the tracker and the ECAL [97]. They are initially identified using an MVA classifier which distinguishes real electrons from hadrons, along with requirements that the track be associated with the collision vertex, and limits on hadronic energy deposits separated by $\Delta R < 0.4$ from the electrons (their "isolation"). The angular separation between two particles is defined as $\Delta R = \sqrt{(\eta_1 - \eta_2)^2 + (\phi_1 - \phi_2)^2}$, where the symbol ϕ refers to the azimuthal direction of the particle. Electrons passing this initial selection are referred to as "loose". In this analysis, events with electrons originating from hadron decays ("nonprompt"), or with hadrons misidentified as electrons, constitute the largest source of background. This motivates the use of an additional MVA classifier, which is trained to select "prompt" electrons

from W, Z, and τ lepton decays, and to reject nonprompt or misidentified electrons. This MVA classifier was previously used for measurements of $\mathrm{t\bar{t}H}$ production in events with multiple leptons [98]. It combines observables comparing measurements of the electron energy and direction in the tracker and the ECAL, the compactness of the electron cluster, the bremsstrahlung emitted along the electron trajectory, and the electron isolation. Two levels of thresholds on the output of this MVA classifier are used in the analysis, referred to as the "tight" and "medium" electron selections for the more and less restrictive thresholds, respectively. The tight selection has an average efficiency of 60% for electrons from SM HH decays. Only the electrons passing the tight selections are used to reconstruct signal candidate events, while data events passing the medium electron selections and failing the tight selections are used to estimate the contribution of misidentified- and nonprompt-electron backgrounds in each search category. Compared to Ref. [98], this analysis uses lower thresholds on the MVA classifier output for the medium and tight electron selections, in order to increase the efficiency in particular for low-p_{T} electrons, which frequently appear in the HH signal events studied in this analysis. Electrons from photon conversions in the tracker are suppressed by requiring that the track is missing no hits in the innermost layers of the silicon tracker, and is not matched to a reconstructed conversion vertex. In the 2ℓss category, further electron selection criteria are applied, which require agreement among three independent measurements of the electron charge, including the Gaussian sum filter and Kalman filter track curvatures, as well as the ECAL supercluster position [99]. The remaining charge misidentification rate is measured to be less than 0.1% for $|\eta| < 1.479$, and under 0.4% for $|\eta| > 1.479$. The charge quality requirement reduces the electron identification efficiency by about 4%.

Muons are reconstructed by extrapolating tracks in the silicon tracker to hits in the gas-ionization muon detectors embedded in the steel flux-return yoke outside the solenoid [100]. To pass the initial loose identification requirement for this analysis, muons must satisfy criteria related to isolation and track proximity to the primary interaction vertex, as well as track quality observables and matching between the tracker and muon chambers. Additional requirements on the prompt vs. nonprompt muon identification MVA classifier from Ref. [98] serve to select muons passing a tight selection for signal candidate events, and a medium selection for nonprompt background estimation. Inputs to this MVA classifier include energy deposits close to the muon in the ECAL and HCAL, the hits and track segments reconstructed in the muon detectors located outside the solenoid, the quality of the spatial matching between the track segments reconstructed in the silicon tracker and in the muon detectors, and the isolation of the muon with respect to other particles. Again, lower selection thresholds on the MVA classifier output compared to Ref. [98] bring higher efficiency for the HH signal, amounting to 80% per muon in simulated SM HH events for the tight selection. In the 2ℓss channel, the uncertainty in the curvature of the muon track is required to be less than 20% to ensure a high-quality charge measurement [98]. This requirement reduces the muon identification efficiency by about 2%.

Hadronic decays of tau leptons are identified using the "hadrons-plus-strips" algorithm [101]. This algorithm classifies individual hadronic decay modes of the τ by combining charged hadrons from the PF reconstruction with neutral pions. The latter are reconstructed by clustering electrons and photons into rectangular strips, which are narrow in η but wide in the ϕ direction. The spread in ϕ accounts for photons originating from neutral pion decays that convert into electron-positron ($\mathrm{e^-e^+}$) pairs while traversing the silicon tracker. The $\mathrm{e^-}$ and $\mathrm{e^+}$ are bent in opposite directions in ϕ by the magnetic field, and may further emit bremsstrahlung photons before reaching the ECAL. The decay modes considered in this analysis produce one charged pion or kaon plus zero to two neutral pions (collectively referred to as "one-prong" τ_{h}), or three charged pions or kaons plus zero or one neutral pion (referred to as "three-prong"

τ_h). The DEEPTAU algorithm [102] distinguishes true τ_h objects from quark and gluon jets, electrons, and muons using a convolutional artificial neural network (ANN) [103] with 42 high-level observables as input, together with low-level information obtained from the silicon tracker, ECAL, HCAL, and the muon detectors. The former include the p_T, η, ϕ, and mass of the τ_h candidate, the reconstructed τ_h decay mode, its isolation with respect to charged and neutral particles, and the estimated distance that the τ lepton traverses between its production and decay. For three-prong τ_h candidates, this distance is determined by reconstructing the decay vertex, while for one-prong τ_h candidates, the transverse impact parameter of the charged pion track with respect to the primary pp interaction vertex is used as an estimate of the distance. The low-level information quantifies the particle activity within two $\eta \times \phi$ grids, centered on the direction of the τ_h candidate: an inner grid of size 0.2×0.2, filled with 0.02×0.02 cells, and an outer grid of size 0.5×0.5 (partially overlapping with the inner grid), with 0.05×0.05 cells. Selected τ_h candidates in this analysis must have $p_T > 20\,\text{GeV}$ and $|\eta| < 2.3$, and are subjected to two levels of thresholds on the output of the ANN that separates τ_h from quark and gluon jets, referred to as the tight and medium τ_h selections, respectively.

Hadronic jets (j) are reconstructed with the anti-k_T algorithm using the particles reconstructed with the PF algorithm as input, and serve to identify $H \to WW \to jj\ell\nu$ decays in this analysis. Jets reconstructed with distance parameters of 0.4 ("small-radius jets") and 0.8 ("large-radius jets") are both used: two small-radius jets to reconstruct the two quarks from low-p_T W boson decays, or a single large-radius jet to reconstruct high-p_T W boson decays, where the quarks are collimated.

The effect of pileup on the reconstruction of large-radius jets is mitigated by applying the pileup per particle identification algorithm (PUPPI) [104, 105] to the collection of particles used as input to the jet reconstruction. Electrons and muons passing the loose selection are also removed from the input collection, so that leptons produced in $H \to WW \to\to jj\ell\nu$ decays of Lorentz-boosted H bosons are not clustered into large-radius jets. For small-radius jets, the effect of pileup is reduced by removing charged particles identified with pileup vertices from the jet reconstruction, and applying corrections to the jet energy to account for neutral particles from pileup. Small-radius jets which contain at least one PF particle matched to an electron, muon, or constituent of a τ_h passing the medium selection criteria are discarded.

After calibration, the jet energy resolution at the central rapidities amounts to 15–20% at 30 GeV, 10% at 100 GeV, and 5% at 1 TeV [106]. This analysis only considers jets reconstructed in the region $|\eta| < 2.4$. Small-radius jets must have $p_T > 25\,\text{GeV}$, while large-radius jets must have $p_T > 170\,\text{GeV}$. Additional criteria requiring that each large-radius jet contain exactly two identifiable, energetic subjets are applied to specifically select those from boosted hadronic W boson decays [107].

Events containing small-radius jets identified with the hadronization of bottom quarks (b jets) are vetoed in this analysis. The DEEPJET algorithm [108] exploits observables related to the long lifetime of b hadrons and the higher particle multiplicity and mass of b jets compared to light quark and gluon jets. Both "loose" and "medium" b jet selections on the DEEPJET output are employed in this analysis, corresponding to b jet selection efficiencies of 84 and 70%, while the misidentification rates for light-quark or gluon jets are 11 and 1.1%, respectively.

The missing transverse momentum vector $\vec{p}_T^{\,\text{miss}}$ is computed as the negative vector p_T sum of all the particles reconstructed by the PF algorithm in an event, and its magnitude is denoted as p_T^{miss} [109]. The $\vec{p}_T^{\,\text{miss}}$ is modified to account for corrections to the energy scale of the reconstructed jets in the event. A linear discriminant, denoted as $p_T^{\text{miss,LD}}$, is employed to remove background events in which the reconstructed p_T^{miss} arises from resolution effects. The discrim-

inant is defined by the relation $p_{\mathrm{T}}^{\mathrm{miss,LD}} = 0.6 p_{\mathrm{T}}^{\mathrm{miss}} + 0.4 H_{\mathrm{T}}^{\mathrm{miss}}$, where $H_{\mathrm{T}}^{\mathrm{miss}}$ corresponds to the magnitude of the vector p_{T} sum of e, μ, and τ_{h} passing the medium selection criteria, and small-radius jets satisfying the criteria detailed above [110].

5 Event selection

Events are selected with the aim of maximizing the acceptance for HH decays to WWWW, WW$\tau\tau$, and $\tau\tau\tau\tau$, while simultaneously rejecting the large backgrounds from multijet production, single and pair production of W and Z bosons, and $\mathrm{t\bar{t}}$ production. To achieve this, we require multiple reconstructed ℓ or τ_{h} to be associated with the primary interaction vertex. The ℓ and τ_{h} may originate from the decay of a W boson or a τ lepton. Seven mutually exclusive search categories, distinguished by the number of reconstructed ℓ and τ_{h} candidates, are included in the analysis: 2ℓss, 3ℓ, 4ℓ, $3\ell + 1\tau_{\mathrm{h}}$, $2\ell + 2\tau_{\mathrm{h}}$, $1\ell + 3\tau_{\mathrm{h}}$, and $4\tau_{\mathrm{h}}$. Here "ss" indicates a same-sign $\ell\ell$ pair, with two leptons of identical electric charge. The ℓ and τ_{h} candidates selected in any of the seven search categories must pass the tight selection criteria described in Section 4. In addition, they are required to pass category-specific p_{T} thresholds motivated by the trigger selection. Further requirements are placed on the sum of ℓ and τ_{h} charges, and, in two categories, on the discriminant $p_{\mathrm{T}}^{\mathrm{miss,LD}}$ and the multiplicity of jets.

The leading and subleading leptons in the 2ℓss category must pass p_{T} selection thresholds of 25 and 15 GeV, respectively. Events in this category are required to contain two or more small-radius jets, or at least one large-radius jet, targeting hadronic W boson decays. Dielectron events must have $p_{\mathrm{T}}^{\mathrm{miss,LD}} > 30$ GeV and $m(\ell\ell) < 81$ GeV or $m(\ell\ell) > 101$ GeV, in order to suppress charge-misidentified $\mathrm{Z} \to \mathrm{ee}$ background. If the event contains a τ_{h}, the charge of the τ_{h} must be opposite to the charge of the leptons. After this selection, the main backgrounds in the 2ℓss category arise from WZ production, from Wγ events in which the photon converts into an $\mathrm{e^-e^+}$ pair and either the $\mathrm{e^-}$ or the $\mathrm{e^+}$ fails to get reconstructed, and from events in which one or both reconstructed leptons are due to a nonprompt ℓ or misidentified hadron, as shown in Table 5. The "other" background given in the table is dominated by same-sign W boson pairs and WWW production. The WWWW decay mode accounts for roughly 70% of SM HH signal events selected in the 2ℓss category, with WW$\tau\tau$ events accounting for the other 30%.

In the 3ℓ category, the leading, subleading, and third ℓ are required to have p_{T} values greater than 25, 15, and 10 GeV, respectively, and the sum of their charges must be either $+1$ or -1. At least one small- or large-radius jet must be present, and the $p_{\mathrm{T}}^{\mathrm{miss,LD}}$ quantity must be greater than 30 GeV, or 45 GeV if there is at least one SFOS $\ell\ell$ pair in the event. Again, backgrounds are dominated by WZ production and events with misidentified ℓ. Notable contributions to the "other" background arise from WWW and WWZ production. The signal composition is similar to the 2ℓss category.

The 4ℓ category has identical lepton selection criteria to the 3ℓ category, except that the third ℓ must have $p_{\mathrm{T}} > 15$ GeV, and a fourth ℓ with $p_{\mathrm{T}} > 10$ GeV is required, and the sum of the four lepton charges is required to be equal to zero. In this category and all the remaining categories, there are no selection requirements on jets or $p_{\mathrm{T}}^{\mathrm{miss,LD}}$. Almost 70% of signal events come from the WWWW decay mode, and about 30% from WW$\tau\tau$, while ZZ production accounts for 85% of the background.

Events in the $3\ell + 1\tau_{\mathrm{h}}$ category are required to satisfy the 3ℓ criteria on the ℓ objects, except that an additional τ_{h} with $p_{\mathrm{T}} > 20$ GeV and charge opposite to the sum of the ℓ charges is required. Background events in which the reconstructed τ_{h} fails a loose selection on the output

of the ANN of the DEEPTAU algorithm that separates τ_h from electrons, or falls near the ECAL barrel-endcap transition region in $1.460 < |\eta| < 1.558$ are removed. About 70% of signal events come from the WW$\tau\tau$ decay mode, while ZZ production and events with at least one misidentified ℓ or τ_h dominate the background.

In the $2\ell + 2\tau_h$ category, the leading and subleading ℓ are required to pass p_T thresholds of 25 and 15 GeV, while the two τ_h must have $p_T > 20$ GeV. The sum of ℓ plus τ_h charges is required to be zero. Signal contributions are mostly from the WW$\tau\tau$ (60%) and $\tau\tau\tau\tau$ (40%) decay modes, while background contributions arise from ZZ production and events with a misidentified ℓ or τ_h candidate.

In the $1\ell + 3\tau_h$ category, the leading ℓ is required to satisfy the conditions $|\eta| < 2.1$ and $p_T > 20$ (15) GeV if it is an electron (muon). The leading, subleading, and third τ_h must have $p_T > 40$, 30, and 20 GeV, respectively, and the sum of τ_h and ℓ charges is required to be zero. Background events containing a $Z \to ee$ decay where one electron is misidentified as a τ_h are vetoed by discarding events containing an e-τ_h pair of opposite charge and mass $71 < m(e\tau_h) < 101$ GeV, and in which the τ_h either fails a loose selection on the discriminant that separates τ_h from electrons, or falls into the region $1.460 < |\eta| < 1.558$. Around 80% of HH signal events selected in the $1\ell + 3\tau_h$ category are from $\tau\tau\tau\tau$ and 20% from the WW$\tau\tau$ decay mode, while the majority of background events stem from ZZ production or contain a misidentified ℓ or τ_h.

The $4\tau_h$ category has identical p_T requirements on the leading three τ_h, and the fourth τ_h is also required to have $p_T > 20$ GeV. Given the extremely low backgrounds in this category, no charge sum criterion or $Z \to ee$ veto is applied. Almost all signal events come from the $\tau\tau\tau\tau$ decay mode, while 55% of the background events contain at least one misidentified τ_h candidate, and the remainder arises from ZZ (30%) and single Higgs boson (15%) production.

In all seven search categories, the background contamination from processes with top quarks is reduced by discarding events with at least one selected small-radius jet passing the medium b jet identification, or at least two passing the loose b jet identification. Leptons originating from low-mass Drell–Yan production, decays of J/ψ and Υ mesons, cascade decays of bottom quarks, and photon conversions are removed by vetoing events containing any pair of loose ℓ with mass $m(\ell\ell) < 12$ GeV. To eliminate overlap with events selected in the ongoing search for HH production in the $b\bar{b}ZZ$, $ZZ \to 4\ell$ decay mode, no event in the 2ℓss, 3ℓ, and 4ℓ categories may contain two same-flavor opposite-sign (SFOS) loose $\ell\ell$ pairs with a combined mass less than 140 GeV. In addition, to reduce the $Z \to \ell\ell$ background, these three categories along with $2\ell + 2\tau_h$ and $3\ell + 1\tau_h$ exclude events where any SFOS loose $\ell\ell$ pair has an invariant mass of 81–101 GeV (Z boson veto).

A summary of the event selection criteria applied in the different categories is given in Table 4. Criteria that are common to all seven search categories are given in Table 3.

The number of events selected in the signal regions of each of the seven search categories, and in two control regions (CRs) which are used to validate the modeling of the WZ and ZZ backgrounds, are given in Table 5. The contribution expected from nonresonant HH production with event kinematics as predicted by the SM, but 30 times the SM cross section, is given separately for HH decays into WWWW, WW$\tau\tau$, and $\tau\tau\tau\tau$ in the upper three rows of each table. The event yields given in the rows labeled WWWW include a small contribution from HH decays into WWZZ and ZZZZ, and, similarly, the numbers quoted in the rows labeled WW$\tau\tau$ include a small contribution from HH decays into ZZ$\tau\tau$. The 3ℓ WZ and 4ℓ ZZ CRs are described in Section 7.

Table 3: Reconstructed object and event selection requirements in all seven search categories. Electrons or muons in the $\ell\ell$ pairs include any leptons passing the loose selection criteria.

Object and event properties	Selection criteria
Lepton and τ_h pseudorapidity	$\lvert\eta\rvert < 2.5$ for e, $\lvert\eta\rvert < 2.4$ for μ, $\lvert\eta\rvert < 2.3$ for τ_h
Dilepton invariant mass	$m_{\ell\ell} > 12\,\text{GeV}$ (all $\ell\ell$ pairs)
Four-lepton invariant mass	$m_{4\ell} > 140\,\text{GeV}$ (any two SFOS $\ell\ell$ pairs)
b jet veto	0 medium and ≤ 1 loose b-tagged small-radius jet

Table 4: Event selection criteria applied in the seven search categories. The p_T thresholds for ℓ and τ_h with the highest, second-, third-, and fourth-highest p_T are separated by slashes. The symbol "—" indicates that no requirement is applied.

Category	2ℓss	3ℓ	4ℓ
Targeted HH decays	WWWW	WWWW	WWWW
Trigger	Single- and double-lepton	Single-, double- and triple-lepton	Single-, double- and triple-lepton
Lepton p_T	>25 / 15 GeV	>25 / 15 / 10 GeV	>25 / 15 / 15 / 10 GeV
Lepton charge sum	± 2, with charge quality requirements applied	± 1	0
Dilepton invariant mass	$\lvert m_{\ell\ell} - m_Z\rvert > 10\,\text{GeV}$ †	$\lvert m_{\ell\ell} - m_Z\rvert > 10\,\text{GeV}$ ‡	$\lvert m_{\ell\ell} - m_Z\rvert > 10\,\text{GeV}$ ‡
Jets	$\geq$2 small-radius jets or $\geq$1 large-radius jet	$\geq$1 small-radius jet or $\geq$1 large-radius jet	—
Missing p_T	$p_T^{\text{miss,LD}} > 30\,\text{GeV}$ §	$p_T^{\text{miss,LD}} > 30\,\text{GeV}$ ‖	—

Category	$3\ell + 1\tau_h$	$2\ell + 2\tau_h$
Targeted HH decays	WW$\tau\tau$	WW$\tau\tau$, $\tau\tau\tau\tau$
Trigger	Single-, double-, and triple-lepton	Single- and double-lepton
Lepton p_T	>25 / 15 / 10 GeV	>25 / 15 GeV
τ_h p_T	>20 GeV	>20 GeV
Lepton and τ_h charge	ℓ and τ_h charges sum to 0	ℓ and τ_h charges sum to 0
Dilepton invariant mass	$\lvert m_{\ell\ell} - m_Z\rvert > 10\,\text{GeV}$ ‡	$\lvert m_{\ell\ell} - m_Z\rvert > 10\,\text{GeV}$ ‡

Category	$1\ell + 3\tau_h$	$4\tau_h$
Targeted HH decays	$\tau\tau\tau\tau$	$\tau\tau\tau\tau$
Trigger	Single-lepton, lepton+τ_h and double-τ_h	Double-τ_h
Lepton η	$\lvert\eta\rvert < 2.1$	—
Lepton p_T	>20 GeV (e) or >15 GeV (μ)	—
τ_h p_T	>40 / 30 / 20 GeV	>40 / 30 / 20 / 20 GeV
Lepton and τ_h charge	ℓ and τ_h charges sum to 0	τ_h charges sum to 0
$Z \to ee$ veto	$\lvert m_{e\tau_h} - 86\,\text{GeV}\rvert > 15\,\text{GeV}$ ¶	—

† Applied to all SFOS $\ell\ell$ pairs and electron pairs with the same charge.

‡ Applied to all SFOS $\ell\ell$ pairs.

§ Only applied to events containing two electrons.

‖ Tightened to $p_T^{\text{miss,LD}} > 45\,\text{GeV}$ if event contains a SFOS $\ell\ell$ pair.

¶ For τ_h classified as electrons by the DeepTau algorithm or with $1.460 < \lvert\eta\rvert < 1.558$.

Table 5: The number of expected and observed events in each of the seven search categories, and in two control regions (CRs), which validate the modeling of the WZ and ZZ backgrounds. The HH signal represents the sum of the ggHH and qqHH production processes and is normalized to 30 times the event yield expected in the SM, corresponding to a cross section of about 1 pb. The expected event yields are computed for the values of nuisance parameters obtained from the ML fit described in Section 9. Quoted uncertainties represent the sum of statistical and systematic components. Uncertainties that are smaller than half the value of the least significant digit have been rounded to zero.

Process	2ℓss	3ℓ	4ℓ
SM HH $\to$ WWWW ($\times$ 30)	73 ± 2	33 ± 1	2.2 ± 0.1
SM HH $\to$ WW$\tau\tau$ ($\times$ 30)	31 ± 1	12 ± 0	1.0 ± 0.1
SM HH $\to \tau\tau\tau\tau$ ($\times$ 30)	3 ± 0	1 ± 0	0.1 ± 0.0
WZ	2003 ± 19	1321 ± 13	0.4 ± 0.1
ZZ	121 ± 1	109 ± 1	54.7 ± 1.6
Misidentified ℓ	3939 ± 83	670 ± 26	2.3 ± 1.0
Conversion electrons	1009 ± 66	146 ± 12	0.9 ± 0.4
Electron charge misid.	366 ± 17	<1	<0.1
Single Higgs boson	$216 \pm$ c2	62 ± 1	2.4 ± 0.3
Other backgrounds	2592 ± 79	249 ± 11	1.1 ± 0.2
Total expected background	$10\,346 \pm 91$	2601 ± 32	64.8 ± 1.8
Data	10 344	2621	62

Process	$3\ell + 1\tau_h$	$2\ell + 2\tau_h$	$1\ell + 3\tau_h$	$4\tau_h$
SM HH $\to$ WWWW ($\times$ 30)	0.9 ± 0.1	0.2 ± 0.0	0.2 ± 0.0	0.3 ± 0.0
SM HH $\to$ WW$\tau\tau$ ($\times$ 30)	4.1 ± 0.2	3.9 ± 0.4	0.6 ± 0.1	0.1 ± 0.0
SM HH $\to \tau\tau\tau\tau$ ($\times$ 30)	0.9 ± 0.0	2.3 ± 0.1	2.6 ± 0.3	1.3 ± 0.2
WZ	0.2 ± 0.0	<0.1	<0.1	<0.1
ZZ	24.3 ± 0.3	18.5 ± 0.4	1.9 ± 0.1	0.7 ± 0.1
Misidentified ℓ and τ_h	25.1 ± 3.1	33.5 ± 3.8	2.1 ± 1.6	1.5 ± 0.9
Conversion electrons	0.1 ± 0.0	0.1 ± 0.1	<0.1	<0.1
Single Higgs boson	3.8 ± 0.2	2.9 ± 0.5	0.8 ± 0.3	0.4 ± 0.1
Other backgrounds	1.1 ± 0.1	1.2 ± 0.2	<0.1	<0.1
Total expected background	56.2 ± 3.3	57.0 ± 3.8	4.9 ± 1.6	2.6 ± 0.9
Data	55	55	6	1

Process	3ℓ WZ CR	4ℓ ZZ CR
WZ	$12\,546 \pm 55$	<1
ZZ	799 ± 7	2032 ± 20
Misidentified ℓ	908 ± 41	13 ± 4
Conversion electrons	134 ± 9	3 ± 0
Other backgrounds	505 ± 17	44 ± 2
Total expected background	$15\,006 \pm 64$	2108 ± 14
Data	14 994	2096

6 Analysis strategy

The rate of the HH signal is extracted through a binned maximum likelihood (ML) fit to the distributions in the output of boosted decision tree (BDT) classifiers [111], which are trained to discriminate the HH signal from backgrounds. The data from each of the three years are fit

separately. Three classifiers are trained for each of the seven search categories using a mix of MC simulation from all three years, targeting nonresonant HH production and resonant HH production from the decay of heavy particles of spin 0 and of spin 2. In the two categories with high event yields (2ℓss and 3ℓ), and in the 4ℓ category, the BDT output binning is chosen such that each bin contains the same number of expected HH signal events. The number of bins is determined by the condition that the relative statistical uncertainty in the background prediction in each bin does not exceed 15%. In the remaining four categories ($3\ell + 1\tau_h$, $2\ell + 2\tau_h$, $1\ell + 3\tau_h$, and $4\tau_h$), which have low event yields, the binning for each BDT output distribution is chosen such that a similar number of expected background events is contained in each bin. Higher bin numbers correspond to a higher BDT output value, and feature a higher signal-to-background ratio. For the SM HH signal, the bins with the highest BDT output values feature a signal-to-background ratio up to 10 times higher than the inclusive ratio in each category.

The inputs to the BDT classifiers include the p_T and η of reconstructed ℓ and τ_h; the angular separation ΔR within $\ell\ell$, $\ell\tau_h$, and $\tau_h\tau_h$ pairs; the ΔR between an ℓ or τ_h candidate and the nearest jet; the number of jets in the event; the discriminant $p_T^{\text{miss,LD}}$; the scalar p_T sum of all reconstructed e, μ, τ_h, and jets; the "visible" mass of the Higgs boson pair, given by the mass of the system of reconstructed e, μ, τ_h, and jets; and the "full" mass of the HH system, including neutrinos, reconstructed using the algorithm described in Ref. [112]. This algorithm targets HH signal events decaying to $\tau\tau\tau\tau$ and thus works best in the $4\tau_h$ and $1\ell + 3\tau_h$ search categories. Distributions in some of the observables used as inputs to the BDT classifiers in the 2ℓss and 3ℓ categories are shown in Fig. 4.

These observables are complemented by further inputs, which allow the BDT to learn that the distributions in the observables for HH signal events change as a function of the model parameters: the Higgs boson couplings λ, y_t, c_g, c_{2g}, and c_2 for nonresonant HH production, and the mass of the heavy particle X in resonant HH production. The training is performed using simulated samples of signal and background events. Background contributions arising from the misidentification of ℓ and τ_h candidates and from the mismeasurement of the electron charge are included in the simulation. When training the BDT that targets nonresonant HH production, the values for the couplings are chosen according to the twelve EFT benchmark scenarios given in Ref. [24]. The BDT for nonresonant HH production is trained on HH samples corresponding to the SM prediction as well as these twelve benchmark scenarios, indicated by thirteen binary inputs to the BDT. The BDT classifiers used for the analysis of resonant HH production are trained on the full set of resonance masses listed in Section 3, and the resonance mass is used as an input to the BDT.

Each simulated background event is replicated thirteen times in the training sample when training the BDT for nonresonant HH production, and nineteen times when training the BDTs that target resonant HH production, setting the binary inputs for the Higgs boson couplings and the mass of the heavy particle X to different values in each duplicate. The number of training events is increased by applying the medium ℓ and τ_h identification criteria instead of the tight ones. Weights are applied to background events arising from different sources, such that the relative fractions of different types of backgrounds in the training match the fractions expected in the signal region of the analysis, i.e. when the tight ℓ and τ_h identification criteria are applied. The MC samples used for the BDT training overlap with the samples used to model signal and background contributions in the analysis. To avoid potential biases, we split the training samples into two samples of equal size, based on even and odd event numbers. The BDTs trained on even events are evaluated on odd events, and vice versa, thereby ensuring that BDT are not trained and evaluated on the same events. The training is performed using the XGBOOST algorithm [113], interfaced to the SCIKIT-LEARN machine learning library [114]. The

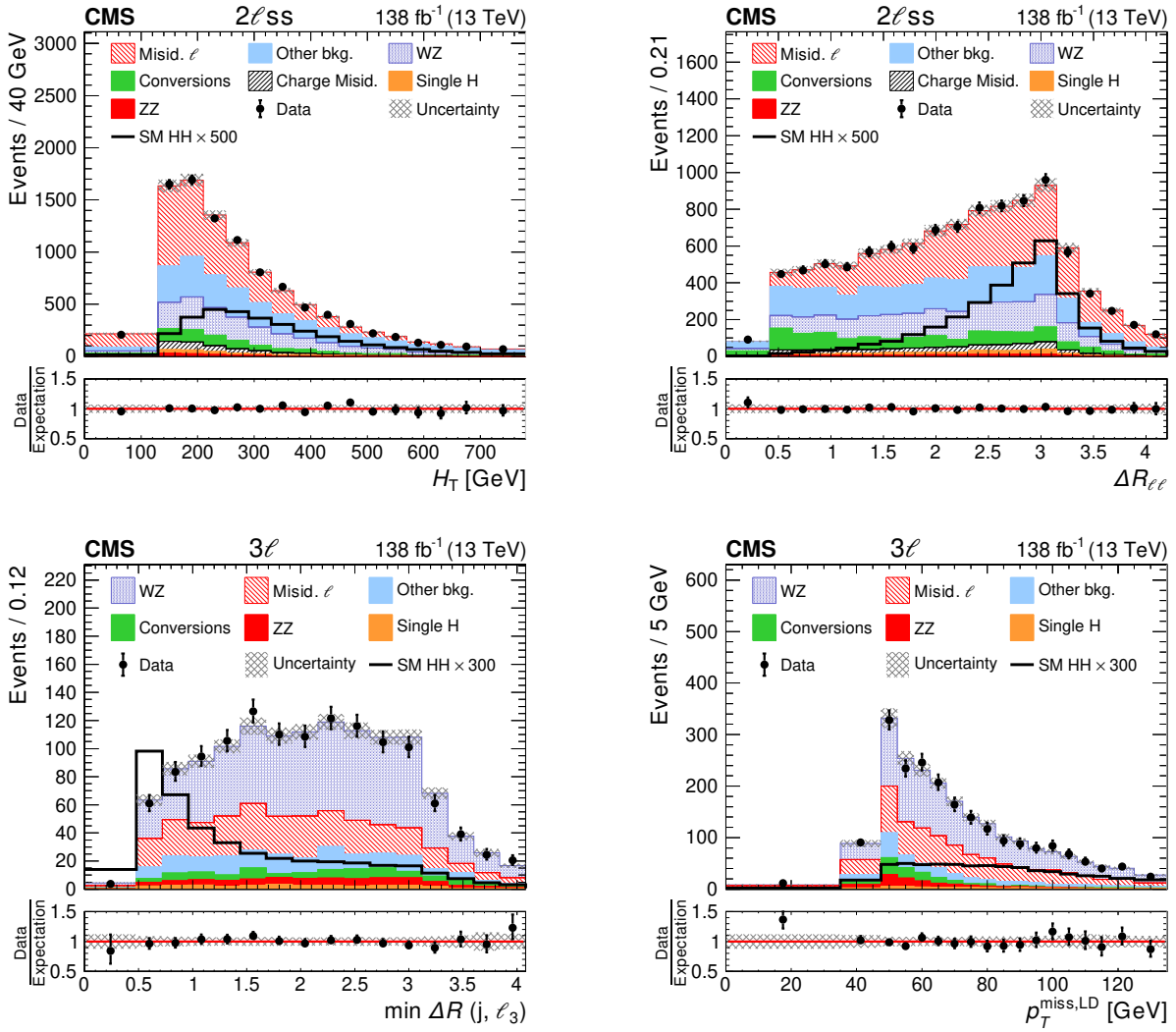

Figure 4: Distributions in a few observables used as inputs to the BDT classifiers in the 2ℓss and 3ℓ categories: the scalar p_T sum, denoted as H_T, of the two reconstructed ℓ and all small-radius jets in the 2ℓss category (upper left); the angular separation ΔR between the two ℓ in the 2ℓss category (upper right); the angular separation between ℓ_3 and the nearest small-radius jet in the 3ℓ category (lower left); and $p_T^{miss,LD}$ in the 3ℓ category (lower right). The ℓ_3 in the 3ℓ category is defined as the ℓ that is not part of the opposite-sign $\ell\ell$ pair of lowest mass. The distributions expected for the different background processes are shown for the values of nuisance parameters obtained from the background-only ML fit, in which the HH signal is constrained to be zero.

parameters of the BDT training (so-called "hyperparameters") are optimized using the particle swarm optimization algorithm described in Ref. [115].

7 Background estimation

Background contributions are classified as either "reducible" or "irreducible". In this analysis, three types of reducible backgrounds are considered, arising from misidentified ℓ or τ_h, electron charge misidentification ("flips"), and electrons from photon conversions. Background events in which all selected ℓ and τ_h come from W, Z, or H boson decays, and are recon-

structed with the correct charge, are considered "irreducible". The ℓ/τ_h misidentification and electron charge misidentification backgrounds are both determined from data, while electron conversions and irreducible backgrounds are modeled using MC simulation.

The ℓ/τ_h misidentification background (which includes nonprompt leptons) is the largest reducible background in all search categories. Nonprompt ℓ are either electrons or muons produced in bottom and charm quark decays, or muons that originate from pion and kaon decays. Hadron jets may also be misidentified as electrons or τ_h. The ℓ/τ_h misidentification background estimate is detailed in Section 7.1. The electron charge misidentification background is only relevant for the 2ℓss search category, and is described in Section 7.2. The modeling of photon conversion events by the MC simulation has been validated in data as described in Ref. [98].

The main contribution to the irreducible background arises from WZ production in the 2ℓss and 3ℓ categories, and ZZ production in the remaining five categories. The production of pairs of bosons (γ, W, Z, or H) other than WZ, ZZ and HH, and production of bosons with top quarks, including Wγ, Zγ, WH, ZH, tH, t$\bar{\text{t}}$H, tW, t$\bar{\text{t}}$W, tZ, t$\bar{\text{t}}$Z, tγ, and t$\bar{\text{t}}\gamma$, constitute subdominant additional backgrounds. The tZ and t$\bar{\text{t}}$Z backgrounds also include contributions from off-shell t$\bar{\text{t}}\gamma^*$ and tγ^* production. Background processes which include at least one top quark are suppressed by the b jet veto described in Section 5, but are still sizable compared to the expected HH signal. All irreducible backgrounds are modeled using the MC simulation.

The modeling of the dominant irreducible WZ and ZZ backgrounds is validated in dedicated CRs, the "3ℓ WZ" CR and "4ℓ ZZ" CR. These CRs are based on the signal regions of the 3ℓ and 4ℓ categories, but with the Z boson veto inverted. The 3ℓ WZ and 4ℓ ZZ CRs are included in the ML fit that is used to extract the HH signal, described in Section 9, thereby providing in-situ constraints on the WZ and ZZ backgrounds and on systematic uncertainties related to lepton identification and trigger efficiency. Distributions in kinematic observables in the 3ℓ WZ and 4ℓ ZZ CRs are shown in Fig. 5. The transverse mass, $m_T = \sqrt{2\, p_T^{\ell}\, p_T^{\text{miss}}\, (1 - \cos\Delta\phi)}$, in the 3ℓ WZ CR is computed using the ℓ that is not identified as originating from the Z boson decay. The symbol $\Delta\phi$ refers to the angle in the transverse plane between the ℓ momentum and the $\vec{p}_T^{\,\text{miss}}$. The observable $m_{4\ell}$ refers to the mass of the 4ℓ system in the 4ℓ ZZ CR.

The modeling of the reducible ℓ/τ_h misidentification background is validated in two further CRs, the "2ℓss CR" and the "$2\ell + 2\tau_h$ CR". They are based on the SRs of the 2ℓss and $2\ell + 2\tau_h$ categories. In the 2ℓss CR, no b jet veto is applied, and at least one small-radius jet passing the medium b jet identification is required. The $2\ell + 2\tau_h$ CR differs from the SR of the $2\ell + 2\tau_h$ category in that the sum of ℓ plus τ_h charges is required to be non-zero, and no Z boson veto is applied. The 2ℓss CR is dominated by events with misidentified ℓ, while the $2\ell + 2\tau_h$ CR is dominated by events with misidentified τ_h. Distributions in the transverse mass m_T in the 2ℓss CR and in the mass of the HH candidate in the $2\ell + 2\tau_h$ CR, reconstructed by the algorithm described in Ref. [112], are shown in Fig. 6. The transverse mass in the 2ℓss CR is computed using the leading ℓ. The data agree well with the background prediction in both CRs.

Simulated events are considered as irreducible background if every selected e, μ, and τ_h candidate matches a prompt MC generator-level counterpart. Events with at least one selected electron from a photon conversion, and the remaining ℓ and τ_h candidates matched to prompt leptons in MC simulation, are classified as conversion background. Electrons that are misidentified as τ_h, and τ_h that are misidentified as e are also modeled using the MC simulation. All other simulated events are discarded, as the ℓ/τ_h misidentification and charge misidentification backgrounds are estimated from data, as described below.

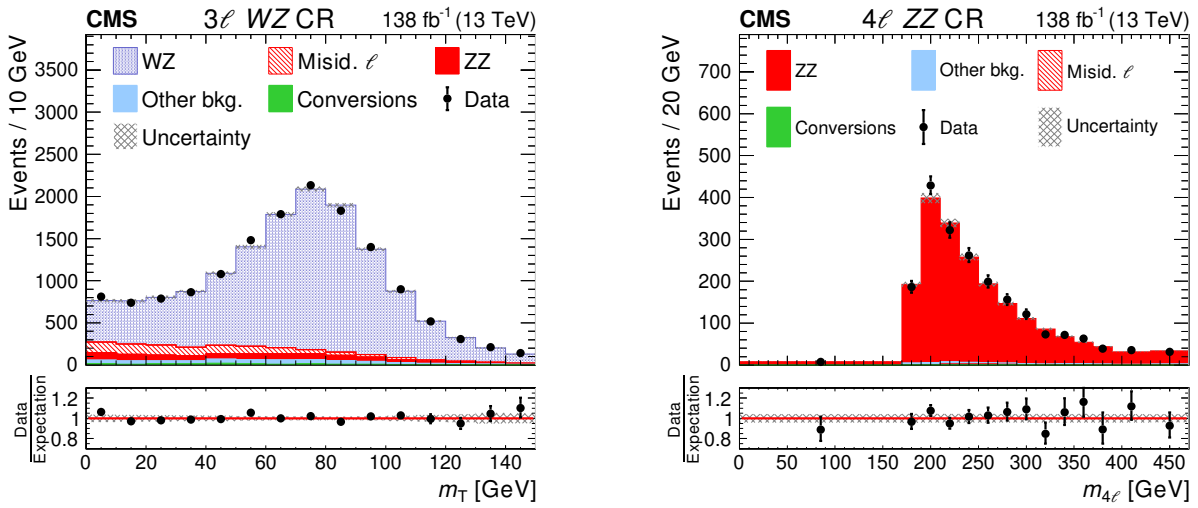

Figure 5: Distributions in m_{T} in the 3ℓ WZ CR (left) and in $m_{4\ell}$ in the 4ℓ ZZ CR (right). The distributions expected for the WZ and ZZ as well as for other background processes are shown for the values of nuisance parameters obtained from the ML fit described in Section 9.

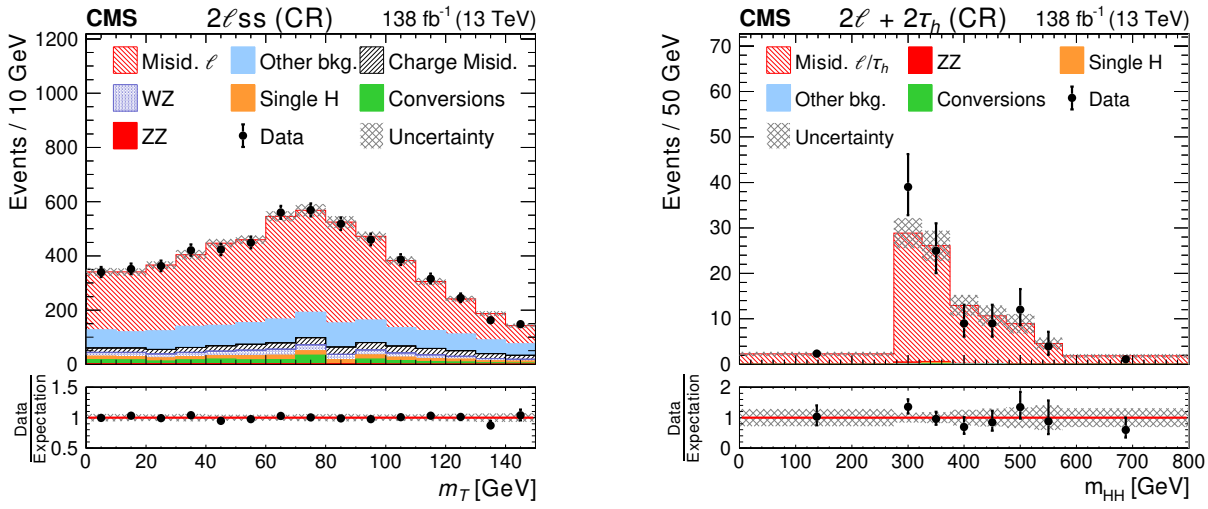

Figure 6: Distributions in m_{T} in the 2ℓss CR (left) and in the mass of the HH candidate in the $2\ell + 2\tau_{\mathrm{h}}$ CR (right). The distributions expected for the misidentified ℓ/τ_{h} background as well as for other background processes are shown for the values of nuisance parameters obtained from the background-only ML fit, in which the HH signal is constrained to be zero.

7.1 Estimation of the misidentification background

The background from events with misidentified ℓ and τ_h candidates is estimated using the "fake factor" or "FF" method from Ref. [110]. An estimate of this background's contribution to the SR of each search category is obtained by selecting a sample of events that satisfy all selection criteria of the SR for the respective search category, except that the e, μ, and τ_h are required to pass the medium selections instead of the tight ones. The sample of events thus obtained is referred to as the application region (AR) of the FF method. Events in which every ℓ and τ_h satisfies the tight selections are excluded from the AR.

The prediction for misidentification backgrounds in the SR is obtained by applying suitably chosen weights w to the events selected in the AR, where w is given by the expression

$$w = (-1)^{n+1} \prod_{i=1}^{n} \frac{f_i(p_T, \eta)}{1 - f_i(p_T, \eta)}. \quad (1)$$

The product extends over all e, μ, and τ_h that pass the medium, but fail the tight selection criteria, and n refers to the total number of such ℓ and τ_h. The symbol $f_i(p_T, \eta)$ corresponds to the probability for a single e, μ, or τ_h that passes the medium selection to also pass the tight one. These probabilities are measured separately for e, μ, and τ_h candidates, and are parametrized as a function of p_T and η. The contributions of irreducible backgrounds to the AR are subtracted based on the MC expectation of such processes. The alternating sign in Eq. (1) is necessary to avoid double-counting arising from events with more than one misidentified ℓ or τ_h [110].

The probabilities $f_i(p_T, \eta)$ for electrons and muons are measured in multijet events, as described in Ref. [98]. The $f_i(p_T, \eta)$ for τ_h are measured using $Z \to \mu\mu$+jets events, where the misidentified τ_h candidates arise from quark or gluon jets. These events are selected by requiring a muon pair passing the tight selection, with opposite charge and invariant mass $60 < m_{\mu\mu} < 120\,\text{GeV}$, plus at least one τ_h candidate that passes the medium τ_h selection. The leading and subleading muons must have $p_T > 25$ and 15 GeV, respectively. Events must also pass the b jet veto described in Section 5 to remove $t\bar{t}$ background.

7.2 Estimation of the charge misidentification background

The electron charge misidentification background in the 2ℓss category is estimated using the method described in Ref. [98]. A sample of dielectron events passing all selection criteria of the SR of the 2ℓss category, except that both electrons are required to have opposite- instead of same-sign charge, is selected and assigned appropriately chosen weights. The weights are computed by summing the probabilities for the charge of either electron to be mismeasured. The probability for the mismeasurement of the electron charge is determined using $Z \to ee$ events, and ranges from under 0.1% in the barrel up to 0.4% in the endcap. The probability for mismeasuring the charge of muons is negligible [98].

8 Systematic uncertainties

Multiple sources of systematic uncertainty affect the predicted event yields, the distributions in the output of the BDT classifiers, or both. These uncertainties may be theoretical, affecting the predicted cross section or decay kinematics of the collision process, or experimental, accounting for differences in object reconstruction and calibration between data and the MC simulation, as well as for uncertainties on the estimates of the ℓ/τ_h misidentification and electron charge misidentification background obtained from data. The systematic uncertainties

may be correlated or uncorrelated across the three data-taking years, and among the various signal and background processes considered in the analysis.

The SM prediction for the ggHH production cross section at $\sqrt{s} = 13\,\text{TeV}$ has a relative uncertainty of $+6.7\%/-23.2\%$, while the qqHH cross section uncertainty is $\pm 2.3\%$. The predicted H boson decay branching fractions to WW, $\tau\tau$, and ZZ have relative uncertainties of 1.54, 1.65, and 1.54%, respectively [116]. Alternate HH predictions are generated with the renormalization and factorization scales varied up and down by a factor of 2. Variations that increase the factorization scale and decrease the renormalization scale (and vice versa) are excluded, following the recommendation of Ref. [116]. All theoretical uncertainties in the HH signal model are correlated across all three data-taking years and among the seven search categories. The uncertainties in the H boson decay branching fractions and the effect of renormalization and factorization scale uncertainties in the signal acceptance impact the measurement of cross sections for nonresonant as well as resonant HH production. Conversely, the uncertainties in the SM prediction for the ggHH and qqHH cross sections only affect the measurement of the HH production rate as a ratio to the SM prediction.

Theoretical uncertainties also affect the irreducible background prediction. The relative uncertainties in the cross sections of the dominant WZ and ZZ backgrounds amount to 2.1 and 6.3%, respectively [117–119]. The uncertainties in the cross section for the subdominant single H boson backgrounds range from 2 to 9% for ggHH, qqHH, WH, and ZH. The cross sections for the production of W, Z, or H bosons with one or two top quarks are known with uncertainties of 8–15%. The event yields of extremely rare backgrounds not mentioned above (e.g., triple boson or four top quark production) are given a conservative uncertainty of 50%, since the analysis has little sensitivity to these processes. Following Ref. [98], background contributions arising from photon conversions are assigned a 30% yield uncertainty. The theoretical uncertainties affecting background cross sections are partially correlated among different processes. Here, contributions arising from uncertainties in the proton PDFs are correlated among processes with a similar initial state. Processes involving single H boson production are an exception. These uncertainties are uncorrelated from other background processes but correlated among each other depending on the initial state. Uncertainties arising from the choice of the renormalization and factorization scales are correlated for processes with similar final states, for example among all processes involving diboson production. Uncertainties in α_s are correlated among all background processes. The theoretical cross section uncertainties for signal processes are uncorrelated with those of background processes, but otherwise follow the same uncertainty scheme for proton PDF, scale, and α_s contributions. All theoretical cross section uncertainties are treated as correlated across the different data-taking years and among all seven search categories.

The rate of the misidentified ℓ/τ_h and electron charge misidentification backgrounds are assigned a 30% uncertainty in all search categories, to account for variations in the misidentification rates between the ARs of the FF method and the multijet ($\text{Z} \to \mu\mu$+jets) event samples used to measure the $f_i(p_\text{T}, \eta)$ for e and μ (τ_h). In the $3\ell + 1\tau_\text{h}$ and $1\ell + 3\tau_\text{h}$ categories, an additional uncertainty of 30% (uncorrelated with the other 30% uncertainty) is assigned to the rate of the misidentified ℓ/τ_h background, to account for the extra uncertainty arising from the modified τ_h selection criteria that suppress the misidentification of electrons as τ_h. The effect of statistical uncertainties in the probabilities $f_i(p_\text{T}, \eta)$ for electrons and muons is evaluated by varying these probabilities in bins of p_T and η and determining the resulting change in the shape of the BDT classifier output distribution obtained for the misidentified ℓ/τ_h background. For τ_h, the effect of statistical uncertainties in $f_i(p_\text{T}, \eta)$ is evaluated by fitting the probabilities in bins of η with functions that are linear in p_T, varying the slope of these functions up and

down within the uncertainties obtained from the fit, and determining the resulting change in the shape of the BDT classifier output distribution.

An additional uncertainty in the BDT output shape in each category is evaluated for events with a nonprompt or misidentified ℓ or τ_h as follows: Simulated events passing all signal selection criteria are compared to those with at least one ℓ or τ_h candidate failing the tight identification criteria, scaled according to the FF method described in Section 7, but with the probabilities $f_i(p_T, \eta)$ taken from the MC simulation instead of from the data. The ratio of these two shapes is fitted with a linear function, which is convoluted with the misidentified ℓ/τ_h background prediction from the data to serve as an uncertainty in the BDT output shape for these events in the SR. The systematic uncertainties associated with the misidentified ℓ/τ_h background prediction and the uncertainty associated with the electron charge misidentification rate are treated as uncorrelated among the different data-taking years.

Uncertainties in the modeling of the trigger and object reconstruction efficiency affect all signal and background processes that are estimated using MC simulation. Trigger efficiencies for events with at least two ℓ are compared between data and MC simulation in control regions enriched in the $t\bar{t}$, WZ, and ZZ background processes, as a function of lepton flavor, p_T, and η. This results in a small p_T-dependent uncertainty correlated between the 2ℓss and $2\ell + 2\tau_h$ categories, and a 1% normalization uncertainty, which is correlated among the 3ℓ, $3\ell + 1\tau_h$, and 4ℓ categories. The data-to-simulation agreement in trigger efficiency for the $4\tau_h$ and $1\ell + 3\tau_h$ categories is computed using an independent set of data, as a function of the p_T and η of the ℓ and all τ_h, and the reconstructed decay modes of all τ_h. The trigger uncertainties for these two categories are treated as uncorrelated. All systematic uncertainties related to trigger modeling are correlated across different physics processes, but uncorrelated among the three data-taking years.

The uncertainties in the reconstruction and identification efficiencies for e, μ, and τ_h candidates have been measured in Z boson enriched regions in data for each level of identification criteria (tight, medium, and loose), and are applied to each event as a function of p_T and η for leptons and of p_T and the reconstructed hadronic decay mode for τ_h. The reconstructed τ_h energy has an uncertainty of around 1%, depending on the data-taking year and reconstructed τ_h decay mode. These uncertainties affect the predicted rate and BDT output shape for signal and background, and are correlated among the different physics processes, but uncorrelated across different data-taking years.

The jet energy scale and resolution are determined using dijet control regions [106, 120]. The jet energy scale is evaluated using 11 separate components, accounting for partial correlations between the data recorded in different years. The jet energy resolution uncertainty is uncorrelated among the three data-taking years. Jet energy uncertainties are also propagated to the p_T^{miss} calculation. An additional uncertainty in $\vec{p}_T^{miss}$ comes from uncertainty in the energy of "unclustered" PF hadrons (PF hadrons not clustered into either small- or large-radius jets), which is uncorrelated across different years. The probability for true b jets to fail the multivariate b jet identification criteria, or for jets from gluons or light flavored quarks to be misidentified as b jets, is compared in data and MC simulation in event regions that are enriched in light-flavor quark or gluon, or heavy-flavor jets. The resulting uncertainty in the data-to-simulation agreement affects the yields and BDT output shapes of multiple physics processes. The statistical component of this uncertainty is treated as uncorrelated across different data-taking years, while other experimental sources are correlated.

The integrated luminosities for data collected in 2016, 2017, and 2018 have 1.2–2.5% individual uncertainties [55–57], while the overall uncertainty for the 2016–2018 period is 1.6%. The

uncertainty in the measured cross section for inelastic pp collisions, amounting to 5% [121], is taken into account by varying the number of pileup interactions in MC simulation, which impacts the jet reconstruction and the isolation of ℓ and τ_h.

The sources of systematic uncertainty which create the largest uncertainties in the measured ratio of the HH production cross section to its SM prediction are the theoretical uncertainties in the HH production cross section and decay branching fractions (25%), the uncertainties in the rate and shape of backgrounds from misidentified ℓ or τ_h (22%), and in the rates of backgrounds modeled using MC simulation (13%). These uncertainties in the signal measurement are determined by removing uncertainties that correspond to a given systematic source from an ML fit to pseudodata, as described in Section 9, and subtracting the obtained uncertainty in the signal measurement in quadrature from the total uncertainty. The impacts of systematic uncertainties are small compared to the effect of the statistical uncertainty in the data (79%), and are comparable to the statistical uncertainties in the distributions in the BDT classifier output for background processes (33%). The latter includes the effect of statistical uncertainties in the MC simulation as well as in the ℓ/τ_h misidentification and electron charge misidentification backgrounds obtained from data. All other sources of uncertainty have an impact of 5% or less.

9 Results

The data selected in the seven search categories are tested against multiple HH production hypotheses: the SM prediction; variations of the SM coupling strength modifiers κ_λ, κ_t, κ_V, and κ_{2V}; the effective couplings c_g, c_{2g}, and c_2 in the EFT approach; and resonant production of H boson pairs originating from the decay of heavy particles with spins of 0 or 2 and masses m_X ranging from 250 to 1000 GeV. In each case, the entire data set is fit simultaneously to a model composed of the background prediction (with uncertainties) and the HH signal hypothesis under consideration. The distributions in m_T in the 3ℓ WZ CR and in $m_{4\ell}$ in the 4ℓ ZZ CR, enriched in WZ and ZZ backgrounds and shown in Fig. 5, are included in each of these fits, in order to obtain in-situ constraints on the systematic uncertainties described in Section 8. This in turn reduces the uncertainties in signal and background predictions in the seven search categories.

The SM "signal strength" parameter μ is defined as the ratio of the measured HH production cross section to its predicted value in the SM. This parameter modifies the expected signal yield by the same proportion in each category. By contrast, variations in the κ modifiers may affect the signal yields in each category differently, and also change the BDT classifier output shape for HH events. The twenty benchmark scenarios spanning combinations of κ_λ, κ_t, c_g, c_{2g}, and c_2 values in the coupling parameter space each correspond to different kinematic distributions, so the HH production cross section for each point is measured separately. Similarly, signal efficiency and BDT classifier output shapes vary dramatically for different resonant masses, and thus a separate measurement is performed for each mass and spin hypothesis. The SM signal strength measurement is performed using the output of the BDT classifier that has been trained for SM nonresonant HH production, while the κ_λ measurement uses the BDT trained for benchmark scenario JHEP04 BM7. In the scenario JHEP04 BM7, the m_{HH} value tends to be close to the lower limit of 250 GeV, which matches the event kinematics for non-resonant HH production in the κ_λ range in which we expect to set the limit. When setting limits on the twenty different benchmark scenarios, the binary BDT inputs correspond to the given scenario, or in case of the benchmarks from Ref. [58] the kinematically closest scenario. In case of resonant HH production, the BDT input for the resonance mass is set to the m_X value for which the limit is computed.

The SM signal strength is measured using a profile likelihood test statistic [122], with systematic uncertainties treated as nuisance parameters θ in a frequentist approach [123]. The effect of variations in θ on the shape of the BDT classifier output distribution for the HH signal and for background processes is incorporated into the ML fit using the technique described in Ref. [124]. Statistical uncertainties in these distributions are also taken into account using the approach detailed in Ref. [124]. The likelihood ratio q_μ for a fixed "test" signal strength value μ is

$$q_\mu = -2\Delta \ln \mathcal{L} = -2 \ln \frac{\mathcal{L}(\text{data}|\mu, \hat{\theta}_\mu)}{\mathcal{L}(\text{data}|\hat{\mu}, \hat{\theta})},$$

where $\hat{\mu}$ and $\hat{\theta}$ are the signal strength and nuisance parameter values that give the maximum value of the likelihood function $\mathcal{L}$ for the given set of data (requiring $\hat{\mu} \geq 0$), and $\hat{\theta}_\mu$ is the set of θ values which maximize $\mathcal{L}$ for the fixed μ. The 95% confidence level (CL) upper limit for μ is obtained using the CL_s criterion [125, 126], with q_μ set to 0 when $\mu < \hat{\mu}$. The probabilities to observe a given value of the likelihood ratio q_μ under the signal-plus-background and background-only hypotheses are computed using the asymptotic approximation from Ref. [122]. The limits on μ obtained using the asymptotic approximation, with all seven search categories and the two CRs for the WZ and ZZ backgrounds fit simultaneously, match the limits obtained with toy MC experiments [123] within 10%. The SM coupling strength modifiers and the cross sections for the various HH production hypotheses are measured by scanning the likelihood ratio q_μ as a function of μ. Theoretical and experimental uncertainties affecting the signal and background yields or the shape of the BDT classifier output distributions may be correlated or uncorrelated across different years, search categories, and BDT output bins, as described in Section 8.

The fits to all BDT output distributions in the data are consistent with the SM background prediction in all search categories, within statistical and systematic uncertainties. Distributions in the output of the BDT classifier for SM nonresonant HH production in the seven search categories are shown in Figs. 7 and 8. The data excess in the rightmost bin of the BDT classifier output distribution for the 3ℓ category is not statistically significant: 11 events are observed in this bin, while 5.2 ± 0.7 are expected from background processes, amounting to a local significance of about 1.7 standard deviations.

For the case of nonresonant HH production with event kinematics as predicted by the SM, the best-fit value of the HH production rate, obtained from the simultaneous fit of all seven search categories with the 3ℓ WZ and 4ℓ ZZ CRs, amounts to $\hat{\mu} = 2 \pm 10$ times the SM expectation. The measured value of the signal strength refers to the sum of ggHH and qqHH production and is compatible with the SM as well as with the background-only hypothesis. The observed (expected) 95% CL upper limit on the cross section for nonresonant HH production is 651 (592) fb. Taking into account the theoretical uncertainties in the SM HH production cross section, this corresponds to an observed (expected) limit on the nonresonant HH production rate of 21.3 (19.4) times the SM expectation. These limits are shown in Fig. 9, for individual categories and for the result obtained from the combination of all seven search categories. The 3ℓ WZ and 4ℓ ZZ CRs are included in all of these fits. We refer to the combined result as the "HH $\rightarrow$ multilepton" result. The 3ℓ and $1\ell + 3\tau_\text{h}$ categories are the most sensitive to SM HH production, followed closely by the other categories.

The observed (expected) 95% CL interval for the H boson trilinear self-coupling strength modifier is measured to be $-6.9 < \kappa_\lambda < 11.1$ ($-6.9 < \kappa_\lambda < 11.7$). The upper limit on κ_λ is one of the strongest constraints on this fundamental SM parameter to date, with only HH searches in the $\text{bb}\gamma\gamma$ [41, 42] and bbbb [43] decay modes providing greater sensitivity. The observed and

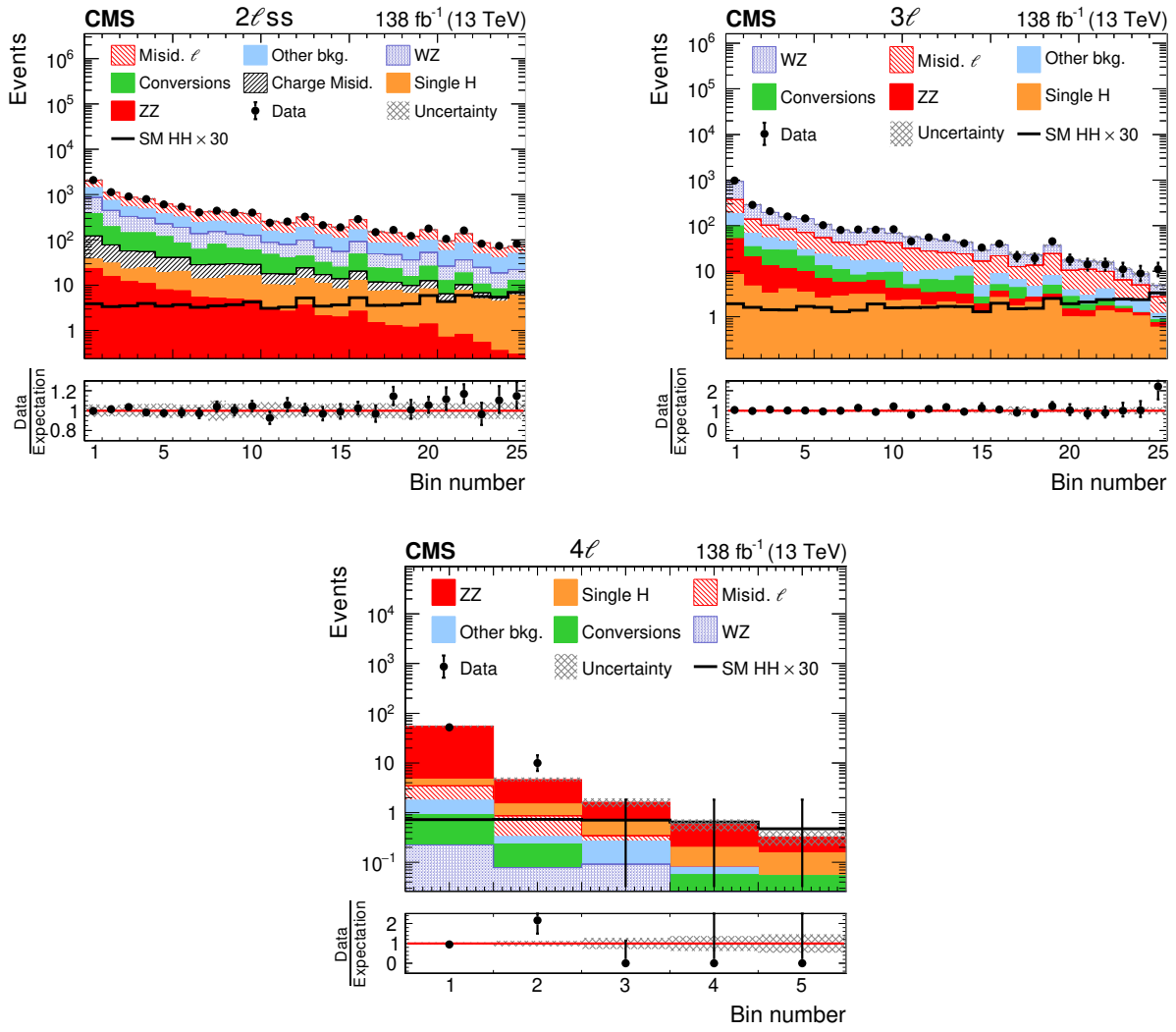

Figure 7: Distribution in the output of the BDT trained for nonresonant HH production and evaluated for the benchmark scenario JHEP04 BM7 for the 2ℓss (upper left), 3ℓ (upper right), and 4ℓ (lower) categories. The SM HH signal is shown for a cross section amounting to 30 times the value predicted in the SM. The distributions expected for the background processes are shown for the values of nuisance parameters obtained from the ML fit of the signal+background hypothesis to the data.

expected upper limits on the HH production cross section as a function of κ_λ, obtained from the simultaneous fit of all seven search categories, are shown in Fig. 10, along with the limits obtained for each category individually. The 3ℓ WZ and 4ℓ ZZ CRs are again included in all of these fits.

The observed and expected limits on the ggHH production cross section for the twenty benchmark scenarios are shown in Fig. 11 and summarized in Table 6. The qqHH process can be safely neglected for these measurements. The observed (expected) limits on nonresonant HH production in the different benchmark scenarios range from 0.21 to 1.09 (0.16 to 1.16) pb, depending on the scenario. These limits are comparable to, but somewhat higher, than those obtained by the CMS measurement in the bb$\gamma\gamma$ final state [41]. The variation in expected limits reflects differences in the m_{HH} distribution among the benchmark scenarios, which in turn affect the p_{T} and angles between the particles produced in the H boson decays. As a con-

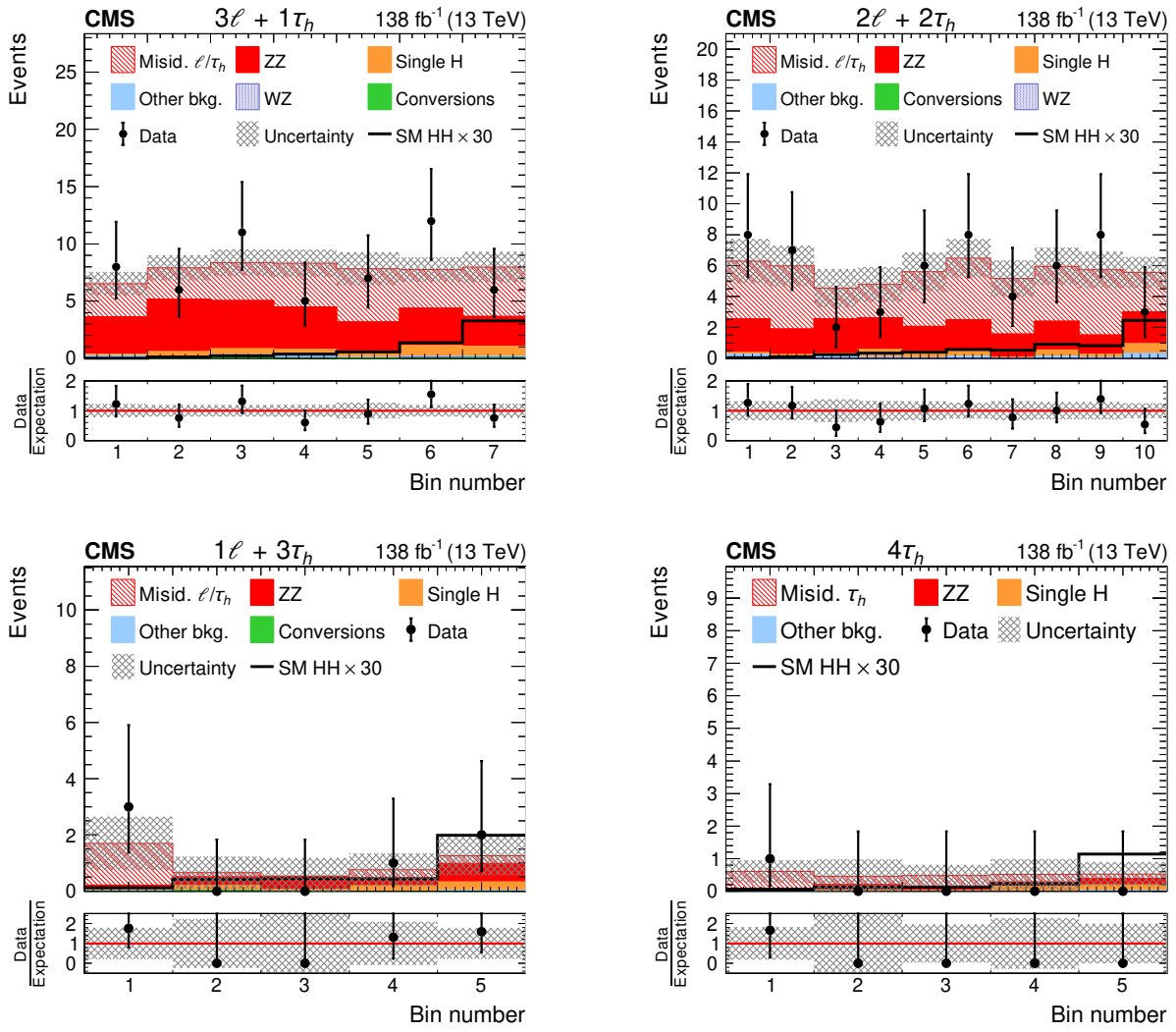

Figure 8: Distribution in the output of the BDT trained for nonresonant HH production and evaluated for the benchmark scenario JHEP04 BM7 for the $3\ell + 1\tau_h$ (upper left), $2\ell + 2\tau_h$ (upper right), $1\ell + 3\tau_h$ (lower left), and $4\tau_h$ (lower right) categories. The SM HH signal is shown for a cross section amounting to 30 times the value predicted in the SM. The distributions expected for the background processes are shown for the values of nuisance parameters obtained from the ML fit of the signal+background hypothesis to the data.

sequence, the signal acceptance can change, as well as the separation of the HH signal from backgrounds through the BDT classifiers described in Section 6. The most and least stringent limits on the cross section are expected for the benchmark scenarios JHEP04 BM2 and BM7, respectively. The former has a pronounced tail of the m_{HH} distribution extending to high values, while the latter is characterized by low m_{HH} values, as seen in Fig. 5 of Ref. [24].

Figure 12 shows the observed and expected upper limits on the HH production cross section as a function of the coupling c_2, and the region excluded in the κ_t–c_2 plane. The effects of variations in κ_λ and κ_t on the rate of the SM single H boson background [21] and on the H boson decay branching fractions [20] are taken into account when computing these limits and those shown in Fig. 10. The magnitude of these effects is typically 5 to 10% within the scanned range of κ_λ and κ_t. Assuming κ_t and κ_λ are both equal to 1, the coupling c_2 is observed (expected) to be constrained to the interval $-1.05 < c_2 < 1.48$ ($-0.96 < c_2 < 1.37$) at 95% CL.

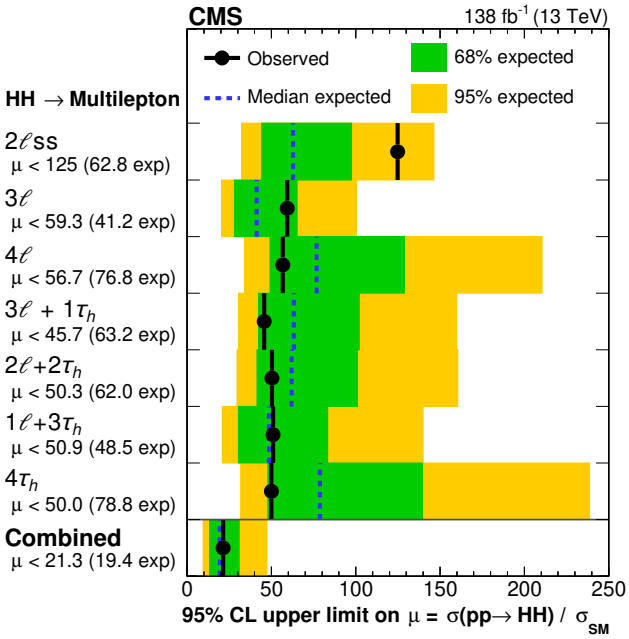

Figure 9: Observed and expected 95% CL upper limits on the SM HH production cross section, obtained for both individual search categories and from a simultaneous fit of all seven categories combined.

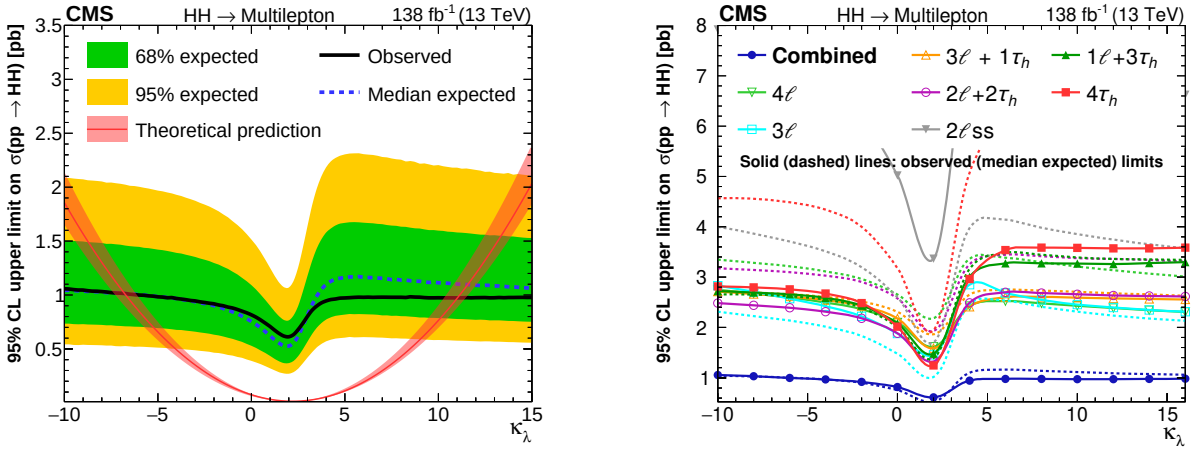

Figure 10: Observed and expected 95% CL upper limits on the HH production cross section as a function of the H boson self-coupling strength modifier κ_λ. All H boson couplings other than λ are assumed to have the values predicted in the SM. The left plot shows the result obtained by combining all seven search categories, while the right plot shows the limits obtained for each category separately. The red curve in the left plot represents the SM prediction for the HH production cross section as a function of κ_λ, and the red shaded band the theoretical uncertainty in this prediction.

Figure 13 shows the observed and expected limits on the resonant HH production cross section as a function of m_X for a spin-0 or spin-2 particle X decaying to HH. The mass points probed are listed in the fourth paragraph of Section 3. The limits are expected to become more stringent as m_X increases, as the acceptance for the HH signal increases and the signal can be more easily distinguished from backgrounds. The observed (expected) 95% CL upper limits on the resonant HH production cross section range from 0.18 to 0.90 (0.08 to 1.06) pb, depending on the mass and spin. Compared to existing combinations of CMS and ATLAS results [50, 51], this

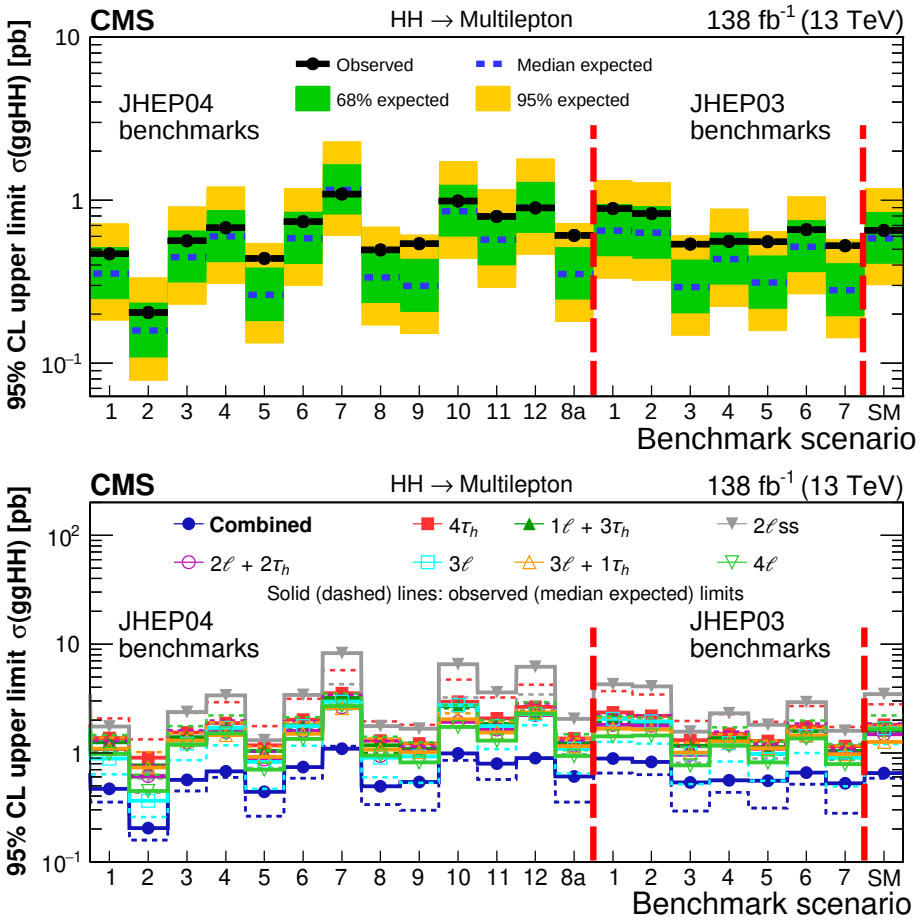

Figure 11: Observed and expected 95% CL upper limits on the HH production cross section for the twelve benchmark scenarios from Ref. [24], the additional benchmark scenario 8a from Ref. [59], the seven benchmark scenarios from Ref. [58], and for the SM. The upper plot shows the result obtained by combining all seven search categories, while the lower plot shows the limits obtained for each category separately, and the combined limit.

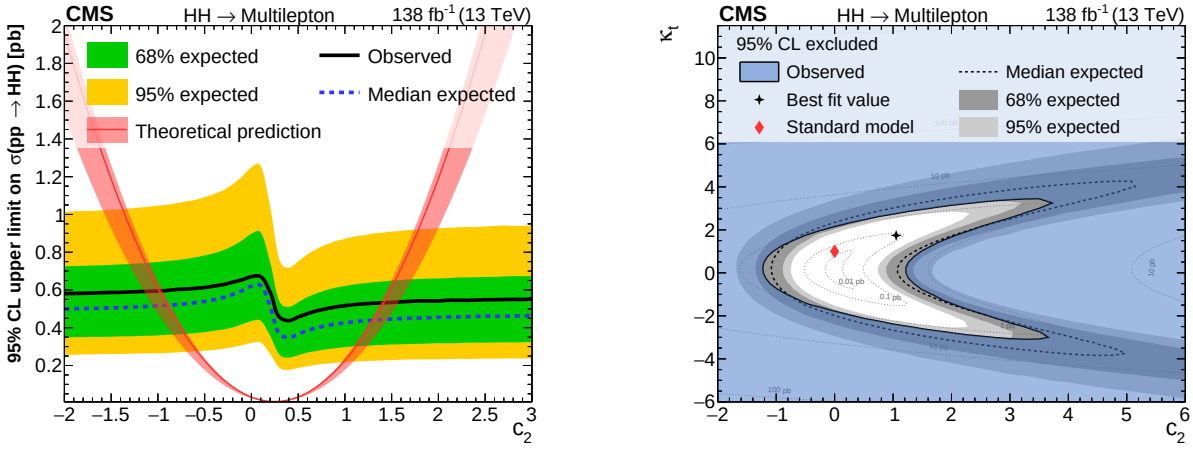

Figure 12: Observed and expected limits on the HH production cross section as a function of the effective coupling c_2 (left), and the region excluded in the κ_t–c_2 plane (right). All limits are computed at 95% CL. H boson couplings other than the ones shown in the plots (c_2 in the left plot and c_2 and κ_t in the right plot) are assumed to have the values predicted by the SM.

Table 6: Observed (expected) 95% CL upper limits on the ggHH production cross section for the twelve benchmark scenarios from Ref. [24], the additional benchmark scenario 8a from Ref. [59] and the seven benchmark scenarios from Ref. [58]. The corresponding observed (expected) upper limit for the SM is 652 (583) fb. The limits correspond to the combination of all seven search categories.

JHEP04 benchmark	Observed (expected) limit [fb]
BM1	469 (354)
BM2	205 (159)
BM3	563 (447)
BM4	677 (600)
BM5	439 (263)
BM6	739 (584)
BM7	1090 (1156)
BM8	495 (336)
BM9	541 (298)
BM10	988 (855)
BM11	795 (572)
BM12	897 (898)
BM8a	608 (353)

JHEP03 benchmark	Observed (expected) limit [fb]
BM1	888 (650)
BM2	828 (632)
BM3	538 (293)
BM4	559 (436)
BM5	556 (313)
BM6	660 (518)
BM7	525 (280)

analysis has superior sensitivity at very low masses (close to 250 GeV), owing to the efficient reconstruction and identification of low-p_{T} leptons in the CMS detector. The recent ATLAS search in the $\mathrm{bb}\gamma\gamma$ final state achieves somewhat lower limits all the way down to 250 GeV [42]. For $m_X \gtrsim 600$ GeV, the observed limit is less stringent than the expected limit, due to a small excess of events in the data that is concentrated near $m_X = 750$ GeV in the 2ℓss and 3ℓ categories. The distributions in the output of the BDT classifier targeting resonances with spin 2 and mass 750 GeV in the 2ℓss and 3ℓ categories are shown in Fig. 14. A small excess of events can be seen in the rightmost bin of both distributions. In the 2ℓss (3ℓ) category, 42 (17) events are observed in this bin in the data, while 27.3 ± 2.9 (8.0 ± 1.0) are expected from background processes, amounting to a local significance of about 2.1 (2.1) standard deviations. The excess affects the observed limits in a broad mass range from 600 to 1000 GeV. The presence of multiple neutrinos in HH signal events in these categories, coming from W boson or τ lepton decays, limits the experimental resolution on m_X and causes the BDT classifier output distributions to be highly correlated for resonances of similar mass. No significant excess is observed in any of the other five search categories. Tabulated results are provided in the HEPData record for this analysis [127].

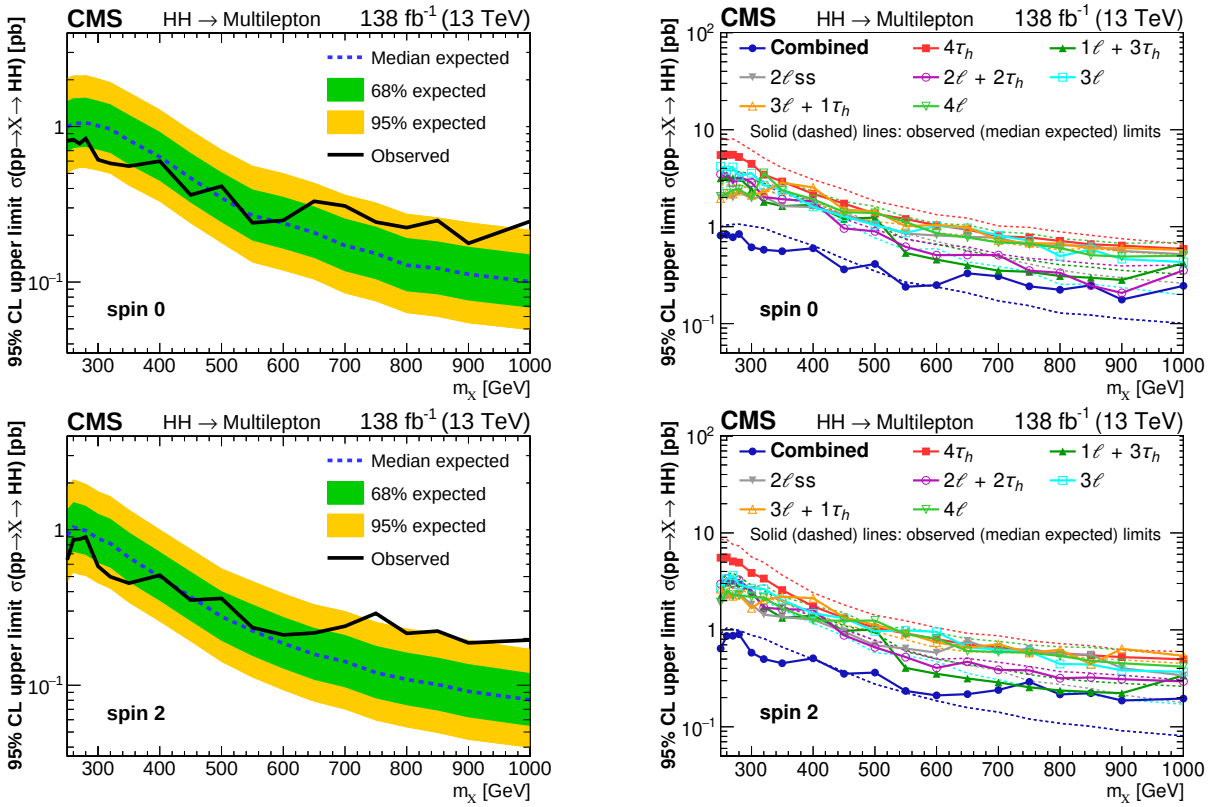

Figure 13: Observed and expected 95% CL upper limits on the production of new particles X of spin 0 (upper) and spin 2 (lower) and mass m_X in the range 250–1000 GeV, which decay to H boson pairs. The plot on the left shows the result obtained by combining all seven search categories, while the plot on the right shows the limits obtained for each category separately, and the combined limit.

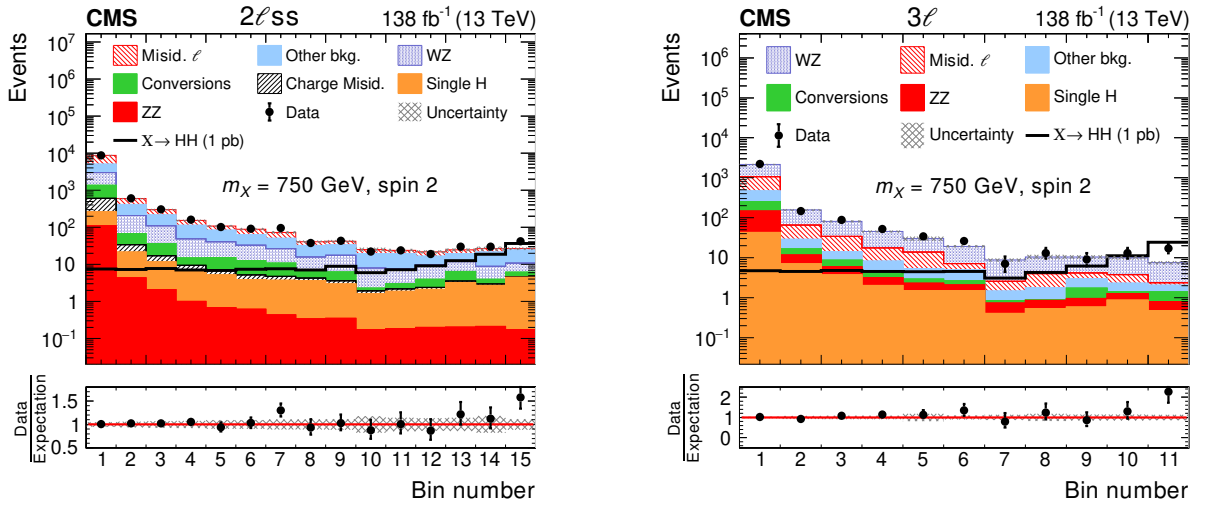

Figure 14: Distribution in BDT classifier output for resonances of spin 2 and mass 750 GeV in the 2ℓss (left) and 3ℓ (right) categories. The resonant HH signal is shown for a cross section amounting to 1 pb. The distributions expected for the background processes are shown for the values of nuisance parameters obtained from the ML fit of the signal+background hypothesis to the data.

10 Summary

The results of a search for nonresonant as well as resonant Higgs boson pair (HH) production in final states with multiple reconstructed leptons, including electrons and muons (ℓ) as well as hadronically decaying tau leptons (τ_h), has been presented. The search targets the HH decay modes WWWW, WW$\tau\tau$, and $\tau\tau\tau\tau$, using proton-proton collision data recorded by the CMS experiment at a center-of-mass energy of 13 TeV and corresponding to an integrated luminosity of 138 fb^{-1}. Seven search categories, distinguished by ℓ and τ_h multiplicity, are included in the analysis: 2ℓss, 3ℓ, 4ℓ, $3\ell + 1\tau_h$, $2\ell + 2\tau_h$, $1\ell + 3\tau_h$, and $4\tau_h$, where "ss" indicates an $\ell\ell$ pair with the same charge. No evidence for a signal is found in the data. Upper limits on the cross section for nonresonant as well as resonant HH production are set. The observed (expected) limits on the nonresonant HH production cross section in twenty EFT benchmark scenarios range from 0.21 to 1.09 (0.16 to 1.16) pb at 95% confidence level (CL), depending on the scenario. For nonresonant HH production with event kinematics as predicted by the standard model (SM), the observed (expected) 95% CL upper limit on the HH production rate is 21.3 (19.4) times the rate expected in the SM. The results of the search for nonresonant HH production are used to exclude regions in the plane of the H boson coupling to the top quark, y_t, and of the trilinear Higgs boson self-coupling, λ. Assuming y_t has the value expected in the SM, the observed (expected) 95% CL interval for λ is between -6.9 and 11.1 (-6.9 and 11.7) times the value expected in the SM. The resonant production of H boson pairs, resulting from decays of new heavy particles X with mass m_X, is probed within the mass range 250–1000 GeV. The corresponding observed (expected) 95% CL upper limits on the cross section for resonant HH production range from 0.18 to 0.90 (0.08 to 1.06) pb, depending on the mass and spin of the resonance.

References

[1] ATLAS Collaboration, "Observation of a new particle in the search for the standard model Higgs boson with the ATLAS detector at the LHC", *Phys. Lett. B* **716** (2012) 1, doi:10.1016/j.physletb.2012.08.020, arXiv:1207.7214.

[2] CMS Collaboration, "Observation of a new boson at a mass of 125 GeV with the CMS experiment at the LHC", *Phys. Lett. B* **716** (2012) 30, doi:10.1016/j.physletb.2012.08.021, arXiv:1207.7235.

[3] CMS Collaboration, "Observation of a new boson with mass near 125 GeV in pp collisions at $\sqrt{s} = 7$ and 8 TeV", *JHEP* **06** (2013) 081, doi:10.1007/JHEP06(2013)081, arXiv:1303.4571.

[4] CMS Collaboration, "Combined measurements of Higgs boson couplings in proton-proton collisions at $\sqrt{s} = 13$ TeV", *Eur. Phys. J. C* **79** (2019) 421, doi:10.1140/epjc/s10052-019-6909-y, arXiv:1809.10733.

[5] ATLAS Collaboration, "Combined measurements of Higgs boson production and decay using up to 80 fb^{-1} of proton-proton collision data at $\sqrt{s} = 13$ TeV collected with the ATLAS experiment", *Phys. Rev. D* **101** (2020) 012002, doi:10.1103/PhysRevD.101.012002, arXiv:1909.02845.

[6] CMS Collaboration, "First evidence for off-shell production of the Higgs boson and measurement of its width", 2022. arXiv:2202.06923. Submitted to *Nature Physics*.

[7] F. Englert and R. Brout, "Broken symmetry and the mass of gauge vector mesons", *Phys. Rev. Lett.* **13** (1964) 321, doi:10.1103/PhysRevLett.13.321.

[8] P. W. Higgs, "Broken symmetries, massless particles and gauge fields", *Phys. Lett.* **12** (1964) 132, doi:10.1016/0031-9163(64)91136-9.

[9] P. W. Higgs, "Broken symmetries and the masses of gauge bosons", *Phys. Rev. Lett.* **13** (1964) 508, doi:10.1103/PhysRevLett.13.508.

[10] G. S. Guralnik, C. R. Hagen, and T. W. B. Kibble, "Global conservation laws and massless particles", *Phys. Rev. Lett.* **13** (1964) 585, doi:10.1103/PhysRevLett.13.585.

[11] P. W. Higgs, "Spontaneous symmetry breakdown without massless bosons", *Phys. Rev.* **145** (1966) 1156, doi:10.1103/PhysRev.145.1156.

[12] T. W. B. Kibble, "Symmetry breaking in non-Abelian gauge theories", *Phys. Rev.* **155** (1967) 1554, doi:10.1103/PhysRev.155.1554.

[13] S. L. Glashow, "Partial symmetries of weak interactions", *Nucl. Phys.* **22** (1961) 579, doi:10.1016/0029-5582(61)90469-2.

[14] S. Weinberg, "A model of leptons", *Phys. Rev. Lett.* **19** (1967) 1264, doi:10.1103/PhysRevLett.19.1264.

[15] A. Salam, "Weak and electromagnetic interactions", *Conf. Proc. C* **680519** (1968) 367, doi:10.1142/9789812795915_0034.

[16] D. de Florian, I. Fabre, and J. Mazzitelli, "Triple Higgs production at hadron colliders at NNLO in QCD", *JHEP* **03** (2020) 155, doi:10.1007/JHEP03(2020)155, arXiv:1912.02760.

[17] O. Aberle et al., "High-Luminosity Large Hadron Collider (HL-LHC): Technical design report V. 0.1", *CERN Yellow Rep. Monogr.* **4** (2017) doi:10.23731/CYRM-2017-004.

[18] M. Grazzini et al., "Higgs boson pair production at NNLO with top quark mass effects", *JHEP* **05** (2018) 059, doi:10.1007/JHEP05(2018)059, arXiv:1803.02463.

[19] F. A. Dreyer and A. Karlberg, "Vector-boson fusion Higgs pair production at N^3LO", *Phys. Rev. D* **98** (2018) 114016, doi:10.1103/PhysRevD.98.114016, arXiv:1811.07906.

[20] G. Degrassi, P. P. Giardino, F. Maltoni, and D. Pagani, "Probing the Higgs self coupling via single Higgs production at the LHC", *JHEP* **12** (2016) 080, doi:10.1007/JHEP12(2016)080, arXiv:1607.04251.

[21] F. Maltoni, D. Pagani, A. Shivaji, and X. Zhao, "Trilinear Higgs coupling determination via single-Higgs differential measurements at the LHC", *Eur. Phys. J. C* **77** (2017) 887, doi:10.1140/epjc/s10052-017-5410-8, arXiv:1709.08649.

[22] W. Buchmuller and D. Wyler, "Effective Lagrangian analysis of new interactions and flavor conservation", *Nucl. Phys. B* **268** (1986) 621, doi:10.1016/0550-3213(86)90262-2.

[23] B. Grzadkowski, M. Iskrzynski, M. Misiak, and J. Rosiek, "Dimension-six terms in the standard model Lagrangian", *JHEP* **10** (2010) 085, doi:10.1007/JHEP10(2010)085, arXiv:1008.4884.

[24] A. Carvalho et al., "Higgs pair production: choosing benchmarks with cluster analysis", *JHEP* **04** (2016) 126, doi:10.1007/JHEP04(2016)126, arXiv:1507.02245.

[25] N. Craig, J. Galloway, and S. Thomas, "Searching for signs of the second Higgs doublet", 2013. arXiv:1305.2424.

[26] D. T. Nhung, M. Mühlleitner, J. Streicher, and K. Walz, "Higher order corrections to the trilinear Higgs self-couplings in the real NMSSM", *JHEP* **11** (2013) 181, doi:10.1007/JHEP11(2013)181, arXiv:1306.3926.

[27] R. Grober and M. Mühlleitner, "Composite Higgs boson pair production at the LHC", *JHEP* **06** (2011) 020, doi:10.1007/JHEP06(2011)020, arXiv:1012.1562.

[28] R. Contino et al., "Strong double Higgs production at the LHC", *JHEP* **05** (2010) 089, doi:10.1007/JHEP05(2010)089, arXiv:1002.1011.

[29] C. Englert, T. Plehn, D. Zerwas, and P. M. Zerwas, "Exploring the Higgs portal", *Phys. Lett. B* **703** (2011) 298, doi:10.1016/j.physletb.2011.08.002, arXiv:1106.3097.

[30] J. M. No and M. Ramsey-Musolf, "Probing the Higgs portal at the LHC through resonant di-Higgs production", *Phys. Rev. D* **89** (2014) 095031, doi:10.1103/PhysRevD.89.095031, arXiv:1310.6035.

[31] L. Randall and R. Sundrum, "A large mass hierarchy from a small extra dimension", *Phys. Rev. Lett.* **83** (1999) 3370, doi:10.1103/PhysRevLett.83.3370, arXiv:hep-ph/9905221.

[32] K. Cheung, "Phenomenology of radion in Randall-Sundrum scenario", *Phys. Rev. D* **63** (2001) 056007, doi:10.1103/PhysRevD.63.056007, arXiv:hep-ph/0009232.

[33] CMS Collaboration, "Search for heavy resonances decaying to a pair of Lorentz-boosted Higgs bosons in final states with leptons and a bottom quark pair at $\sqrt{s}$ = 13 TeV", 2021. arXiv:2112.03161. Submitted to *JHEP*.

[34] ATLAS Collaboration, "Search for pair production of Higgs bosons in the $\mathrm{b\bar{b}b\bar{b}}$ final state using proton-proton collisions at $\sqrt{s} = 13$ TeV with the ATLAS detector", *JHEP* **01** (2019) 030, doi:10.1007/JHEP01(2019)030, arXiv:1804.06174.

[35] U. Baur, T. Plehn, and D. L. Rainwater, "Measuring the Higgs boson self-coupling at the LHC and finite top mass matrix elements", *Phys. Rev. Lett.* **89** (2002) 151801, doi:10.1103/PhysRevLett.89.151801, arXiv:hep-ph/0206024.

[36] U. Baur, T. Plehn, and D. L. Rainwater, "Determining the Higgs boson self-coupling at hadron colliders", *Phys. Rev. D* **67** (2003) 033003, doi:10.1103/PhysRevD.67.033003, arXiv:hep-ph/0211224.

[37] Q. Li, Z. Li, Q.-S. Yan, and X. Zhao, "Probe Higgs boson pair production via the $3\ell\,2\mathrm{j} + p_{\mathrm{T}}^{\mathrm{miss}}$ mode", *Phys. Rev. D* **92** (2015) 014015, doi:10.1103/PhysRevD.92.014015, arXiv:1503.07611.

[38] A. Adhikary et al., "Revisiting the non-resonant Higgs pair production at the HL-LHC", *JHEP* **07** (2018) 116, doi:10.1007/JHEP07(2018)116, arXiv:1712.05346.

[39] J. Ren et al., "LHC search of new Higgs boson via resonant di-Higgs production with decays into 4W", *JHEP* **06** (2018) 090, doi:10.1007/JHEP06(2018)090, arXiv:1706.05980.

[40] ATLAS Collaboration, "Search for Higgs boson pair production in the WW^*WW^* decay channel using ATLAS data recorded at $\sqrt{s} = 13$ TeV", *JHEP* **05** (2019) 124, doi:10.1007/JHEP05(2019)124, arXiv:1811.11028.

[41] CMS Collaboration, "Search for nonresonant Higgs boson pair production in final states with two bottom quarks and two photons in proton-proton collisions at $\sqrt{s} = 13$ TeV", *JHEP* **03** (2021) 257, doi:10.1007/JHEP03(2021)257, arXiv:2011.12373.

[42] ATLAS Collaboration, "Search for Higgs boson pair production in the two bottom quarks plus two photons final state in pp collisions at $\sqrt{s} = 13$ TeV with the ATLAS detector", 2021. arXiv:2112.11876. Submitted to *Phys. Rev. D.*

[43] CMS Collaboration, "Search for Higgs boson pair production in the four b quark final state in proton-proton collisions at $\sqrt{s}$ = 13 TeV", 2022. arXiv:2202.09617. Submitted to *Phys. Rev. Lett.*

[44] CMS Collaboration, "Search for resonant pair production of Higgs bosons decaying to bottom quark-antiquark pairs in proton-proton collisions at 13 TeV", *JHEP* **08** (2018) 152, doi:10.1007/JHEP08(2018)152, arXiv:1806.03548.

[45] CMS Collaboration, "Search for Higgs boson pair production in events with two bottom quarks and two tau leptons in pp collisions at $\sqrt{s} = 13$ TeV", *Phys. Lett. B* **778** (2018) 101, doi:10.1016/j.physletb.2018.01.001, arXiv:1707.02909.

[46] ATLAS Collaboration, "Search for resonant and non-resonant Higgs boson pair production in the $b\bar{b}\tau^+\tau^-$ decay channel in pp collisions at $\sqrt{s} = 13$ TeV with the ATLAS detector", *Phys. Rev. Lett.* **121** (2018), no. 19, 191801, doi:10.1103/PhysRevLett.121.191801, arXiv:1808.00336. [Erratum: doi:10.1103/PhysRevLett.122.089901].

[47] CMS Collaboration, "Search for resonant and non-resonant Higgs boson pair production in the $b\bar{b}\ell\nu\ell\nu$ final state in proton-proton collisions at $\sqrt{s} = 13$ TeV", *JHEP* **01** (2018) 054, doi:10.1007/JHEP01(2018)054, arXiv:1708.04188.

[48] ATLAS Collaboration, "Search for non-resonant Higgs boson pair production in the $b\bar{b}\ell\nu\ell\nu$ final state with the ATLAS detector in pp collisions at $\sqrt{s} = 13$ TeV", *Phys. Lett. B* **801** (2020) 135145, doi:10.1016/j.physletb.2019.135145, arXiv:1908.06765.

[49] ATLAS Collaboration, "Search for Higgs boson pair production in the $\gamma\gamma WW^*$ channel using pp collision data recorded at $\sqrt{s} = 13$ TeV with the ATLAS detector", *Eur. Phys. J. C* **78** (2018) 1007, doi:10.1140/epjc/s10052-018-6457-x, arXiv:1807.08567.

[50] CMS Collaboration, "Combination of searches for Higgs boson pair production in proton-proton collisions at $\sqrt{s} = 13$ TeV", *Phys. Rev. Lett.* **122** (2019) 121803, doi:10.1103/PhysRevLett.122.121803, arXiv:1811.09689.

[51] ATLAS Collaboration, "Combination of searches for Higgs boson pairs in pp collisions at $\sqrt{s} = 13$ TeV with the ATLAS detector", *Phys. Lett. B* **800** (2020) 135103, doi:10.1016/j.physletb.2019.135103, arXiv:1906.02025.

[52] CMS Collaboration, "Performance of the CMS level-1 trigger in proton-proton collisions at $\sqrt{s} = 13\,\text{TeV}$", *JINST* **15** (2020) P10017, doi:10.1088/1748-0221/15/10/P10017, arXiv:2006.10165.

[53] CMS Collaboration, "The CMS trigger system", *JINST* **12** (2017) P01020, doi:10.1088/1748-0221/12/01/P01020, arXiv:1609.02366.

[54] CMS Collaboration, "The CMS experiment at the CERN LHC", *JINST* **3** (2008) S08004, doi:10.1088/1748-0221/3/08/S08004.

[55] CMS Collaboration, "Precision luminosity measurement in proton-proton collisions at $\sqrt{s} = 13\,\text{TeV}$ in 2015 and 2016 at CMS", *Eur. Phys. J. C* **81** (2021) 800, doi:10.1140/epjc/s10052-021-09538-2, arXiv:2104.01927.

[56] CMS Collaboration, "CMS luminosity measurement for the 2017 data-taking period at $\sqrt{s} = 13\,\text{TeV}$", CMS Physics Analysis Summary CMS-PAS-LUM-17-004, 2018.

[57] CMS Collaboration, "CMS luminosity measurement for the 2018 data-taking period at $\sqrt{s} = 13\,\text{TeV}$", CMS Physics Analysis Summary CMS-PAS-LUM-18-002, 2019.

[58] M. Capozi and G. Heinrich, "Exploring anomalous couplings in Higgs boson pair production through shape analysis", *JHEP* **03** (2020) 091, doi:10.1007/JHEP03(2020)091, arXiv:1908.08923.

[59] G. Buchalla et al., "Higgs boson pair production in non-linear effective field theory with full m_t-dependence at NLO QCD", *JHEP* **09** (2018) 057, doi:10.1007/JHEP09(2018)057, arXiv:1806.05162.

[60] A. Carvalho et al., "On the reinterpretation of non-resonant searches for Higgs boson pairs", *JHEP* **02** (2021) 049, doi:10.1007/JHEP02(2021)049, arXiv:1710.08261.

[61] J. Alwall et al., "The automated computation of tree-level and next-to-leading order differential cross sections, and their matching to parton shower simulations", *JHEP* **07** (2014) 079, doi:10.1007/JHEP07(2014)079, arXiv:1405.0301.

[62] A. Kalogeropoulos and J. Alwall, "The SysCalc code: A tool to derive theoretical systematic uncertainties", 1, 2018. arXiv:1801.08401.

[63] P. Nason, "A new method for combining NLO QCD with shower Monte Carlo algorithms", *JHEP* **11** (2004) 040, doi:10.1088/1126-6708/2004/11/040, arXiv:hep-ph/0409146.

[64] S. Frixione, P. Nason, and C. Oleari, "Matching NLO QCD computations with parton shower simulations: The powheg method", *JHEP* **11** (2007) 070, doi:10.1088/1126-6708/2007/11/070, arXiv:0709.2092.

[65] S. Alioli, P. Nason, C. Oleari, and E. Re, "A general framework for implementing NLO calculations in shower Monte Carlo programs: The POWHEG BOX", *JHEP* **06** (2010) 043, doi:10.1007/JHEP06(2010)043, arXiv:1002.2581.

[66] T. Melia, P. Nason, R. Rontsch, and G. Zanderighi, "W^+W^-, WZ and ZZ production in the POWHEG BOX", *JHEP* **11** (2011) 078, doi:10.1007/JHEP11(2011)078, arXiv:1107.5051.

[67] P. Nason and G. Zanderighi, "W^+W^-, WZ and ZZ production in the POWHEG-BOX-V2", *Eur. Phys. J. C* **74** (2014) 2702, doi:10.1140/epjc/s10052-013-2702-5, arXiv:1311.1365.

[68] J. M. Campbell, R. K. Ellis, P. Nason, and E. Re, "Top-pair production and decay at NLO matched with parton showers", *JHEP* **04** (2015) 114, doi:10.1007/JHEP04(2015)114, arXiv:1412.1828.

[69] S. Alioli, S.-O. Moch, and P. Uwer, "Hadronic top-quark pair-production with one jet and parton showering", *JHEP* **01** (2012) 137, doi:10.1007/JHEP01(2012)137, arXiv:1110.5251.

[70] S. Alioli, P. Nason, C. Oleari, and E. Re, "NLO single-top production matched with shower in POWHEG: *s*- and *t*-channel contributions", *JHEP* **09** (2009) 111, doi:10.1088/1126-6708/2009/09/111, arXiv:0907.4076. [Erratum: doi:10.1007/JHEP02(2010)011].

[71] E. Re, "Single-top *Wt* production matched with parton showers using the POWHEG method", *Eur. Phys. J. C* **71** (2011) 1547, doi:10.1140/epjc/s10052-011-1547-z, arXiv:1009.2450.

[72] R. Frederix, E. Re, and P. Torrielli, "Single-top *t*-channel hadroproduction in the four-flavour scheme with POWHEG and aMC@NLO", *JHEP* **09** (2012) 130, doi:10.1007/JHEP09(2012)130, arXiv:1207.5391.

[73] S. Alioli, P. Nason, C. Oleari, and E. Re, "NLO Higgs boson production via gluon fusion matched with shower in POWHEG", *JHEP* **04** (2009) 002, doi:10.1088/1126-6708/2009/04/002, arXiv:0812.0578.

[74] P. Nason and C. Oleari, "NLO Higgs boson production via vector-boson fusion matched with shower in POWHEG", *JHEP* **02** (2010) 037, doi:10.1007/JHEP02(2010)037, arXiv:0911.5299.

[75] K. Mimasu, V. Sanz, and C. Williams, "Higher order QCD predictions for associated Higgs production with anomalous couplings to gauge bosons", *JHEP* **08** (2016) 039, doi:10.1007/JHEP08(2016)039, arXiv:1512.02572.

[76] G. Heinrich et al., "NLO predictions for Higgs boson pair production with full top quark mass dependence matched to parton showers", *JHEP* **08** (2017) 088, doi:10.1007/JHEP08(2017)088, arXiv:1703.09252.

[77] G. Heinrich et al., "Probing the trilinear Higgs boson coupling in di-Higgs production at NLO QCD including parton shower effects", *JHEP* **06** (2019) 066, doi:10.1007/JHEP06(2019)066, arXiv:1903.08137.

[78] J. Davies et al., "Double Higgs boson production at NLO: Combining the exact numerical result and high-energy expansion", *JHEP* **11** (2019) 024, doi:10.1007/JHEP11(2019)024, arXiv:1907.06408.

[79] G. Heinrich, S. P. Jones, M. Kerner, and L. Scyboz, "A non-linear EFT description of $gg \to HH$ at NLO interfaced to POWHEG", *JHEP* **10** (2020) 021, doi:10.1007/JHEP10(2020)021, arXiv:2006.16877.

[80] T. Sjöstrand et al., "An introduction to PYTHIA 8.2", *Comput. Phys. Commun.* **191** (2015) 159, doi:10.1016/j.cpc.2015.01.024, arXiv:1410.3012.

[81] B. Hespel, D. Lopez-Val, and E. Vryonidou, "Higgs pair production via gluon fusion in the two-Higgs-doublet model", *JHEP* **09** (2014) 124, doi:10.1007/JHEP09(2014)124, arXiv:1407.0281.

[82] A. Carvalho, "Gravity particles from warped extra dimensions, predictions for LHC", 3, 2014. arXiv:1404.0102.

[83] NNPDF Collaboration, "Parton distributions for the LHC Run II", *JHEP* **04** (2015) 040, doi:10.1007/JHEP04(2015)040, arXiv:1410.8849.

[84] NNPDF Collaboration, "Parton distributions from high-precision collider data", *Eur. Phys. J. C* **77** (2017) 663, doi:10.1140/epjc/s10052-017-5199-5, arXiv:1706.00428.

[85] J. Butterworth et al., "PDF4LHC recommendations for LHC Run II", *J. Phys. G* **43** (2016) 023001, doi:10.1088/0954-3899/43/2/023001, arXiv:1510.03865.

[86] J. Rojo et al., "The PDF4LHC report on PDFs and LHC data: Results from Run I and preparation for Run II", *J. Phys. G* **42** (2015) 103103, doi:10.1088/0954-3899/42/10/103103, arXiv:1507.00556.

[87] A. Accardi et al., "A critical appraisal and evaluation of modern PDFs", *Eur. Phys. J. C* **76** (2016) 471, doi:10.1140/epjc/s10052-016-4285-4, arXiv:1603.08906.

[88] CMS Collaboration, "Event generator tunes obtained from underlying event and multiparton scattering measurements", *Eur. Phys. J. C* **76** (2016) 155, doi:10.1140/epjc/s10052-016-3988-x, arXiv:1512.00815.

[89] CMS Collaboration, "Extraction and validation of a new set of CMS PYTHIA8 tunes from underlying-event measurements", *Eur. Phys. J. C.* **80** (2020) 4, doi:10.1140/epjc/s10052-019-7499-4, arXiv:1903.12179.

[90] P. Skands, S. Carrazza, and J. Rojo, "Tuning PYTHIA 8.1: The Monash 2013 tune", *Eur. Phys. J. C* **74** (2014) 3024, doi:10.1140/epjc/s10052-014-3024-y, arXiv:1404.5630.

[91] J. Alwall et al., "Comparative study of various algorithms for the merging of parton showers and matrix elements in hadronic collisions", *Eur. Phys. J. C* **53** (2008) 473, doi:10.1140/epjc/s10052-007-0490-5, arXiv:0706.2569.

[92] R. Frederix and S. Frixione, "Merging meets matching in MC@NLO", *JHEP* **12** (2012) 061, doi:10.1007/JHEP12(2012)061, arXiv:1209.6215.

[93] GEANT4 Collaboration, "GEANT4: A simulation toolkit", *Nucl. Instrum. Meth. A* **506** (2003) 250, doi:10.1016/S0168-9002(03)01368-8.

[94] CMS Collaboration, "Particle-flow reconstruction and global event description with the CMS detector", *JINST* **12** (2017) P10003, doi:10.1088/1748-0221/12/10/P10003, arXiv:1706.04965.

[95] M. Cacciari, G. P. Salam, and G. Soyez, "The anti-k_{T} jet clustering algorithm", *JHEP* **04** (2008) 063, doi:10.1088/1126-6708/2008/04/063, arXiv:0802.1189.

[96] M. Cacciari, G. P. Salam, and G. Soyez, "FASTJET user manual", *Eur. Phys. J. C* **72** (2012) 1896, doi:10.1140/epjc/s10052-012-1896-2, arXiv:1111.6097.

[97] CMS Collaboration, "Electron and photon reconstruction and identification with the CMS experiment at the CERN LHC", *JINST* **16** (2021), no. 05, P05014, doi:10.1088/1748-0221/16/05/P05014, arXiv:2012.06888.

[98] CMS Collaboration, "Measurement of the Higgs boson production rate in association with top quarks in final states with electrons, muons, and hadronically decaying tau leptons at $\sqrt{s} = 13\,\text{TeV}$", *Eur. Phys. J. C* **81** (2021) 378, doi:10.1140/epjc/s10052-021-09014-x, arXiv:2011.03652.

[99] CMS Collaboration, "Performance of electron reconstruction and selection with the CMS detector in pp collisions at $\sqrt{s} = 8\,\text{TeV}$", *JINST* **10** (2015) P06005, doi:10.1088/1748-0221/10/06/P06005, arXiv:1502.02701.

[100] CMS Collaboration, "Performance of the CMS muon detector and muon reconstruction with proton-proton collisions at $\sqrt{s} = 13\,\text{TeV}$", *JINST* **13** (2018) P06015, doi:10.1088/1748-0221/13/06/P06015, arXiv:1804.04528.

[101] CMS Collaboration, "Performance of reconstruction and identification of τ leptons decaying to hadrons and ν_τ in pp collisions at $\sqrt{s} = 13\,\text{TeV}$", *JINST* **13** (2018) P10005, doi:10.1088/1748-0221/13/10/P10005, arXiv:1809.02816.

[102] CMS Collaboration, "Identification of hadronic tau lepton decays using a deep neural network", 1, 2022. arXiv:2201.08458. Submitted to JINST.

[103] Y. LeCun, "Generalization and network design strategies", in *Connectionism in perspective*, R. Pfeifer, Z. Schreter, F. Fogelman, and L. Steels, eds. Elsevier, Zurich, Switzerland, 1989. An extended version was published as a technical report of the University of Toronto.

[104] CMS Collaboration, "Pileup mitigation at CMS in 13 TeV data", *JINST* **15** (2020) P09018, doi:10.1088/1748-0221/15/09/p09018, arXiv:2003.00503.

[105] D. Bertolini, P. Harris, M. Low, and N. Tran, "Pileup per particle identification", *JHEP* **10** (2014) 059, doi:10.1007/JHEP10(2014)059, arXiv:1407.6013.

[106] CMS Collaboration, "Jet energy scale and resolution in the CMS experiment in pp collisions at 8 TeV", *JINST* **12** (2017) P02014, doi:10.1088/1748-0221/12/02/P02014, arXiv:1607.03663.

[107] CMS Collaboration, "Search for resonances decaying to a pair of Higgs bosons in the $\mathrm{b\bar{b}q\bar{q}'}\ell\nu$ final state in proton-proton collisions at $\sqrt{s} = 13\,\text{TeV}$", *JHEP* **10** (2019) 125, doi:10.1007/JHEP10(2019)125, arXiv:1904.04193.

[108] E. Bols et al., "Jet flavour classification using DeepJet", *JINST* **15** (2020), no. 12, P12012, doi:10.1088/1748-0221/15/12/P12012, arXiv:2008.10519.

[109] CMS Collaboration, "Performance of missing transverse momentum reconstruction in proton-proton collisions at $\sqrt{s} = 13\,\text{TeV}$ using the CMS detector", *JINST* **14** (2019) P07004, doi:10.1088/1748-0221/14/07/P07004, arXiv:1903.06078.

[110] CMS Collaboration, "Evidence for associated production of a Higgs boson with a top quark pair in final states with electrons, muons, and hadronically decaying τ leptons at $\sqrt{s} = 13\,\text{TeV}$", *JHEP* **08** (2018) 066, doi:10.1007/JHEP08(2018)066, arXiv:1803.05485.

[111] L. Breiman, J. Friedman, R. A. Olshen, and C. J. Stone, "Classification and regression trees". Chapman and Hall/CRC, 1984. ISBN 978-0-412-04841-8.

[112] K. Ehatäht, L. Marzola, and C. Veelken, "Reconstruction of the mass of Higgs boson pairs in events with Higgs boson pairs decaying into four τ leptons", 9, 2018. arXiv:1809.06140.

[113] T. Chen and C. Guestrin, "XGBOOST: A scalable tree boosting system", in *Proceedings of the 22nd ACM SIGKDD International Conference on Knowledge Discovery and Data Mining*, p. 785. ACM, New York, NY, USA, 2016. arXiv:1603.02754. doi:10.1145/2939672.2939785.

[114] F. Pedregosa et al., "SCIKIT-LEARN: Machine learning in Python", *J. Mach. Learn. Res.* **12** (2011) 2825, arXiv:1201.0490.

[115] L. Tani, D. Rand, C. Veelken, and M. Kadastik, "Evolutionary algorithms for hyperparameter optimization in machine learning for application in high energy physics", *Eur. Phys. J. C* **81** (2021) 170, doi:10.1140/epjc/s10052-021-08950-y, arXiv:2011.04434.

[116] LHC Higgs Cross Section Working Group, "Handbook of LHC Higgs Cross Sections: 4. Deciphering the nature of the Higgs sector", *CERN Yellow Rep. Monogr.* **2** (2017) doi:10.23731/CYRM-2017-002, arXiv:1610.07922.

[117] M. Grazzini, S. Kallweit, D. Rathlev, and M. Wiesemann, "$W^{\pm}Z$ production at hadron colliders in NNLO QCD", *Phys. Lett. B* **761** (2016) 179, doi:10.1016/j.physletb.2016.08.017, arXiv:1604.08576.

[118] F. Cascioli et al., "ZZ production at hadron colliders in NNLO QCD", *Phys. Lett. B* **735** (2014) 311, doi:10.1016/j.physletb.2014.06.056, arXiv:1405.2219.

[119] Caola, F. and Melnikov, K. and Rontsch, R. and Tancredi, L., "QCD corrections to ZZ production in gluon fusion at the LHC", *Phys. Rev. D* **92** (2015), no. 9, 094028, doi:10.1103/PhysRevD.92.094028, arXiv:1509.06734.

[120] CMS Collaboration, "Jet algorithms performance in 13 TeV data", CMS Physics Analysis Summary CMS-PAS-JME-16-003, 2017.

[121] CMS Collaboration, "Measurement of the inelastic proton-proton cross section at $\sqrt{s} = 13\,\text{TeV}$", *JHEP* **07** (2018) 161, doi:10.1007/JHEP07(2018)161, arXiv:1802.02613.

[122] G. Cowan, K. Cranmer, E. Gross, and O. Vitells, "Asymptotic formulae for likelihood-based tests of new physics", *Eur. Phys. J. C* **71** (2011) 1554, doi:10.1140/epjc/s10052-011-1554-0, arXiv:1007.1727. [Erratum: doi:10.1140/epjc/s10052-013-2501-z].

[123] ATLAS and CMS Collaborations, and LHC Higgs Combination Group, "Procedure for the LHC Higgs boson search combination in summer 2011", technical report, 2011.

[124] J. S. Conway, "Incorporating nuisance parameters in likelihoods for multisource spectra", in *PHYSTAT 2011*, p. 115. 2011. arXiv:1103.0354. doi:10.5170/CERN-2011-006.115.

[125] T. Junk, "Confidence level computation for combining searches with small statistics", *Nucl. Instrum. Meth. A* **434** (1999) 435, doi:10.1016/S0168-9002(99)00498-2, arXiv:hep-ex/9902006.

[126] A. L. Read, "Presentation of search results: The CL_s technique", *J. Phys. G* **28** (2002) 2693, doi:10.1088/0954-3899/28/10/313.

[127] HEPData record for this analysis, 2022. doi:10.17182/hepdata.130795.